Sebastian Strasser, BSc

Precise orbit determination of GNSS satellites using the raw observation approach

MASTER'S THESIS

to achieve the university degree of

Diplom-Ingenieur

Master's degree programme: Geomatics Science

submitted to

Graz University of Technology

Supervisor

Univ.-Prof. Dr.-Ing. Torsten Mayer-Gürr

Institute of Geodesy

Graz, April 2016

AFFIDAVIT

I declare that I have authored this thesis independently, that I have not used other than the declared sources/resources, and that I have explicitly indicated all material which has been quoted either literally or by content from the sources used. The text document uploaded to TUGRAZonline is identical to the present master‘s thesis.

Date

Signature

Abstract

Global navigation satellite systems (GNSS) play an increasingly important role in the economy, society, and in science. Many applications, e.g. Precise Point Positioning (PPP), require highly precise GNSS satellite orbits. Such orbits are routinely determined by analysis centers of the International GNSS Service (IGS). The aim of this thesis was the determination of precise GNSS satellite orbits using the raw observation approach. This new approach offers some benefits compared to well-established approaches, such as a straightforward incorporation of new observables due to the avoidance of observation differences and linear combinations. This becomes especially important in view of the changing GNSS landscape with two new systems currently in deployment. Modeling the forces acting on GNSS satellites is a fundamental part of GNSS orbit determination. Numerical analyses showed that while some small conservative forces are negligible, proper modeling of nonconservative forces, most importantly solar radiation pressure, is crucial. Within the scope of this thesis, Global Positioning System (GPS) satellite orbits were determined over a period of nine years using observations from the global IGS station network. The results demonstrated that the raw observation approach is applicable to orbit determination of GNSS satellites. Some areas requiring further work have been identified, enabling future improvements of the method.

Kurzfassung

Globale Satellitennavigationssysteme (GNSS) spielen eine immer wichtigere Rolle in der Wirtschaft, Gesellschaft und Wissenschaft. Viele Applikationen, z.B. Precise Point Positioning (PPP), benötigen hochpräzise GNSS-Satellitenorbits. Diese werden regelmäßig von den Analysezentren des International GNSS Service (IGS) bestimmt. Ziel dieser Arbeit war die Bestimmung präziser GNSS-Satellitenorbits unter Verwendung des Raw-Observation-Ansatzes. Dieser neue Ansatz bietet einige Vorteile gegenüber etablierten Ansätzen, z.B. eine unkomplizierte Einbindung neuer Beobachtungtypen, da Beobachtungsdifferenzen und Linearkombinationen vermieden werden. Dieser Aspekt ist im Hinblick auf aktuelle Entwicklungen im Bereich von GNSS, etwa der derzeitigen Einführung von zwei neuen Satellitensystemen, besonders wichtig. Die Modellierung von Kräften, die auf GNSS-Satelliten wirken, ist ein wesentlicher Teil der GNSS-Orbitbestimmung. In numerischen Analysen zeigte sich, dass einige kleine konservative Kräfte vernachlässigbar sind. Die korrekte Modellierung von nichtkonservativen Kräften, im Besonderen des Strahlungsdrucks der Sonne, ist jedoch äußerst wichtig. Im Rahmen dieser Arbeit wurden Satellitenorbits des Global Positioning Systems (GPS) über einen Zeitraum von neun Jahren aus Beobachtungen des globalen IGS-Stationsnetzwerks bestimmt. Die Ergebnisse zeigten, dass der Raw-Observation-Ansatz zur Orbitbestimmung von GNSS-Satelliten verwendbar ist. In manchen Bereichen wurde die Notwendigkeit von weiteren Arbeiten erkannt, die zukünftige Verbesserungen des Ansatzes ermöglichen.

Acknowledgements

First and foremost, I would like to thank my supervisor, Univ.-Prof. Dr.-Ing. Torsten Mayer-Gürr, for giving me the opportunity to work on this topic. I very much appreciate his support, advice, patience, and the time he spent on our countless discussions. The knowledge and experience I gained during my work on this thesis and my time at the institute are invaluable to me.

Special thanks go to Norbert Zehentner for his preceding work, which formed the foundation of this thesis, and for answering the many questions that arose throughout my work. Furthermore, I would like to thank the staff of the working group Theoretical Geodesy and Satellite Geodesy of the Institute of Geodesy for all their support.

Finally, I wish to thank my parents, family, and friends for supporting me throughout my life and always being there for me.

Contents

Introduction

1

The importance of global navigation satellite systems (GNSS) for scientific research as well as commercial and noncommercial applications has been rapidly increasing in the recent past. This becomes evident by the introduction of two new and independent GNSS, the European system Galileo and the Chinese system BeiDou. While satellite broadcast ephemeris cover the majority of use cases for the general population, high-precision applications require highly precise GNSS satellite orbits. Precise orbits are regularly determined and published by the analysis centers of the International GNSS Service (IGS). The current processing methods of the analysis centers make use of the ionosphere-free linear combination to reduce the ionospheric influence. Some of the analysis centers also form observation differences, in general double-differences, to eliminate several additional error sources. While forming linear combinations or differences has benefits in terms of error reduction, inherent drawbacks are an increased measurement noise and a reduced number of available observations.

The aim of this thesis is to apply the raw observation approach to precise orbit determination of GNSS satellites in an effort to avoid the drawbacks mentioned above. The raw observation approach was introduced by Zehentner and Mayer-Gürr (2014) for kinematic orbit determination of low Earth orbit (LEO) satellites. Contrary to other approaches, this approach directly uses all available observations in one least squares adjustment without forming linear combinations or differences. Consequently, this requires the correction of all known influences in advance using state-of-the-art models. All remaining influences that cannot be modeled sufficiently have to be included as additional parameters in the least squares adjustment.

This thesis is structured as follows: Chapter 2 provides a general overview of GNSS, including important aspects like different satellite models and available observables. It also contains a brief summary of the IGS and its products. Chapter 3 covers orbit modeling, the associated force models, and variational equations, which are used during linearization of the GNSS observation equations. In Chapter 4, the raw observation approach is described in detail, including models and corrections that have to be applied to the observation equations when this approach is used. Numerical analyses of the effects of different force models on GNSS orbits are presented in Chapter 5. Chapter 6 focuses on precise orbit determination using observations from a global network of permanent stations. It also covers the data, models, and settings used in the processing. The resulting orbits are validated against IGS final orbits to make a statement about their quality. Finally, Chapter 7 summarizes the analyses and results and provides an outlook on possible future improvements.

2

Global navigation satellite systems

For the last three decades, the U.S. Global Positioning System (GPS) and the Russian Globalnaya Navigatsionnaya Sputnikovaya Sistema (GLONASS) have been the primary satellite systems for global positioning, navigation, and timing. The rapidly increasing economical, societal, and political importance of GNSS has resulted in the European system Galileo and the Chinese system BeiDou, two new and independent systems with global coverage. GPS and GLONASS are currently fully operational, with both systems undergoing modernization in terms of new satellite models and signals. Galileo and BeiDou are still in the deployment phase, with full operational capability (FOC) for both systems currently scheduled for 2020 (Montenbruck et al., 2014). Table 2.1 provides a brief comparison of important system parameters for GPS, GLONASS, Galileo, and BeiDou. More detailed information about these systems can be found in Hofmann-Wellenhof et al. (2008). The global systems are augmented by autonomous regional systems like the Indian Regional Navigation Satellite System (IRNSS) and regional space-based augmentation systems (SBAS) like the European Geostationary Navigation Overlay Service (EGNOS). These regional systems are not covered in this thesis.

Tab. 2.1: System parameters for GPS, GLONASS, Galileo, and BeiDou (Hofmann-Wellenhof et al., 2008; China Satellite Navigation Office, 2013; International GNSS Service, 2015)

Characteristic	**GPS**	**GLONASS**	**Galileo**	**BeiDou**
Nominal satellites	24	24	27	27/3/5[1]
Orbital planes	6	3	3	3
Orbit inclination	55°	64.8°	56°	55°
Semimajor axis	26 560 km	25 508 km	29 601 km	27 878 km
Plane separation	60°	120°	120°	120°
Revolution peroid	∼11 h 58 min	∼11 h 16 min	∼14 h 5 min	∼12 h 53 min
Ground track repeat	∼1 day	∼8 days	∼10 days	∼7 days
Reference system[2]	WGS84	PE-90	GTRF	CGCS2000
Time system	GPS Time	GLONASS Time	GST	BeiDou Time
Signal separation[3]	CDMA	FDMA	CDMA	CDMA
Number of freq.	3	3[4]	4	3
Frequencies [MHz]	L1: 1575.420	G1: 1602.000	E1: 1575.420	B1: 1561.098
	L2: 1227.600	G2: 1246.000	E5a: 1176.450	B2: 1207.140
	L5: 1176.450	G3: 1202.025	E5b: 1207.140	B3: 1268.520
			E6: 1278.750	

---

[1] The nominal BeiDou constellation consists of 27 medium Earth orbit (MEO), three inclined geosynchronous orbit (IGSO) and five geostationary orbit (GEO) satellites.

[2] Abbrev.: World Geodetic System 1984 (WGS84), Parameters of the Earth 1990 (PE-90), Galileo Terrestrial Reference Frame (GTRF), China Geodetic Coordinate System 2000 (CGCS2000), Galileo System Time (GST)

[3] Abbrev.: code division multiple access (CDMA), frequency division multiple access (FDMA)

[4] GLONASS has one frequency set per two antipodal satellites due to frequency division multiple access.

2.1 Satellite models and observables

In the past, both GPS and GLONASS only offered five observables (disregarding Doppler measurements) on two frequencies: a civil code on one frequency, a protected code on each frequency and the phase of each signal. With the modernization of both systems and the introduction of Galileo and BeiDou, the number of potential observables for a GNSS receiver has increased drastically. GPS block IIR-M added a second civil code on L2 and new military (M) codes on both frequencies. The new block IIF satellites transmit an additional civil signal on L5 and thus are the first GPS satellites that transmit on three frequencies (Global Positioning Systems Directorate, 2013). The new GLONASS K satellites will also add a third frequency and furthermore introduce code division multiple access (CDMA) in addition to the currently used frequency division multiple access (FDMA) technique (Oleynik, 2012).

More observables offer many benefits, e.g. for ambiguity resolution (Wang and Rothacher, 2013) or cycle-slip detection and repair (Zhao et al., 2015). On the other hand, more observables also increase the complexity of receiver design, software implementation, and data processing (Montenbruck et al., 2014). Table 2.2 gives an overview of the observables provided by the different satellite models of each system. A historical overview of the number of operational GNSS satellites grouped by system and model is shown in Figure 2.1. Currently, there are three GPS, two GLONASS, two Galileo, and three BeiDou satellite models active. They do not only differ in signals but also in terms of spacecraft design. This aspect has to be accounted for in orbit modeling, e.g. regarding solar and Earth radiation pressure.

Tab. 2.2: GNSS satellite models and phase/code observables in RINEX 3.03 nomenclature (International GNSS Service, 2015; Global Positioning Systems Directorate, 2013; Russian Institute of Space Device Engineering, 2008; European Union, 2010; Montenbruck et al., 2014)

Sat. model	**Phase**	**Code**
GPS I	L1*, L2*	C1C, C1P, C2P
GPS II	L1*, L2*	C1C, C1P, C2P
GPS IIA	L1*, L2*	C1C, C1P, C2P
GPS IIR	L1*, L2*	C1C, C1P, C2P
GPS IIR-M	L1*, L2*	C1C, C1P, C1M, C2C, C2P, C2M
GPS IIF	L1*, L2*, L5*	C1C, C1P, C1M, C2C, C2P, C2M, C5I, C5Q
GLONASS I	L1*, L2*	C1C, C1P, C2P
GLONASS IIa	L1*, L2*	C1C, C1P, C2P
GLONASS IIb	L1*, L2*	C1C, C1P, C2P
GLONASS IIv	L1*, L2*	C1C, C1P, C2P
GLONASS M	L1*, L2*	C1C, C1P, C2C, C2P
GLONASS K1	L1*, L2*, L3*	C1C, C1P, C2C, C2P, C3I, C3Q
Galileo IOV	L1*, L5*, L6*, L7*	C1A, C1B, C1C, C5I, C5Q, C6A, C6B, C6C, C7I, C7Q
Galileo FOC	L1*, L5*, L6*, L7*	C1A, C1B, C1C, C5I, C5Q, C6A, C6B, C6C, C7I, C7Q
BeiDou GEO	L2*, L6*, L7*	C2I, C2Q, C6I, C6Q, C7I, C7Q
BeiDou IGSO	L2*, L6*, L7*	C2I, C2Q, C6I, C6Q, C7I, C7Q
BeiDou MEO	L2*, L6*, L7*	C2I, C2Q, C6I, C6Q, C7I, C7Q

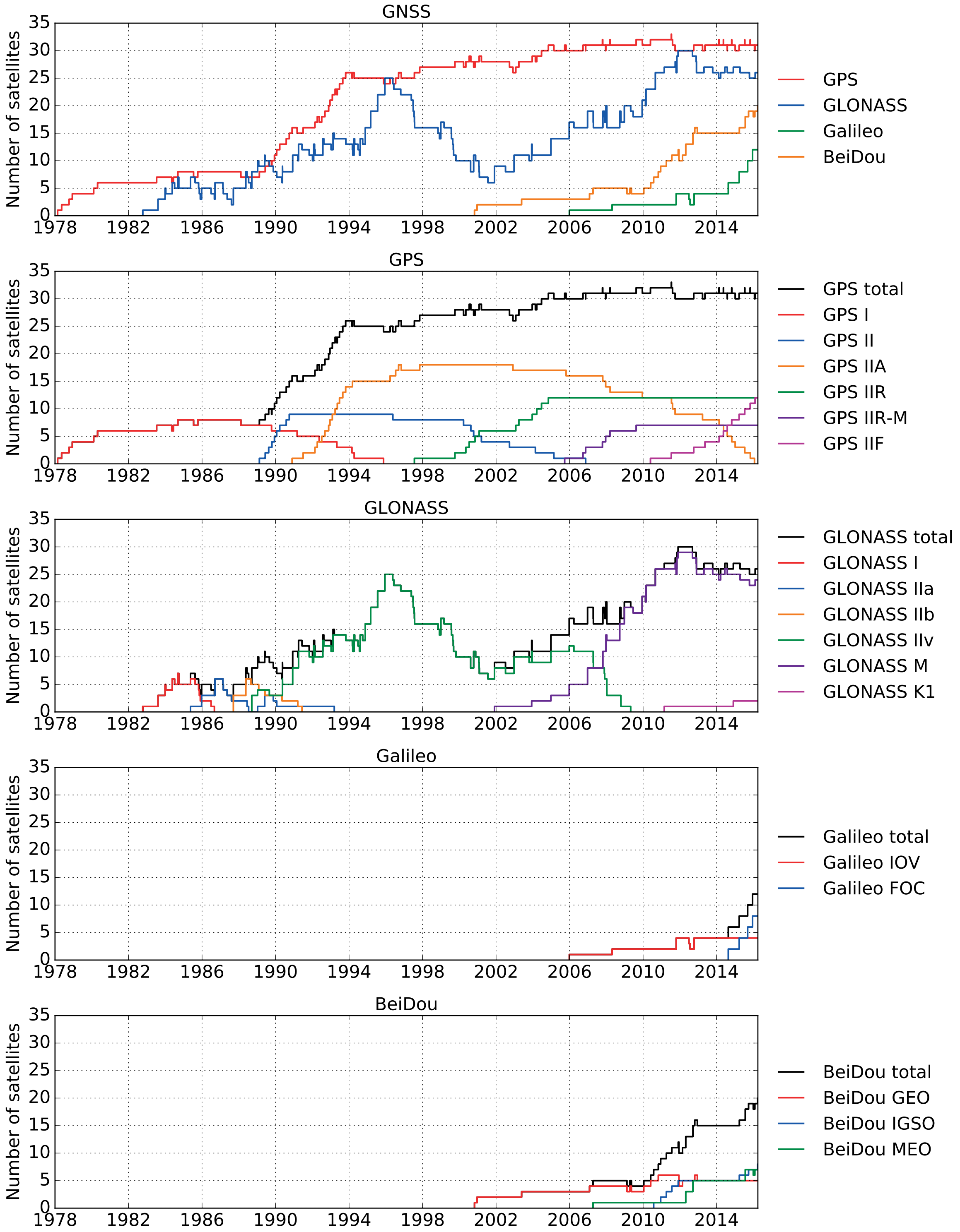

Fig. 2.1: Historical overview of the number of operational GNSS satellites for the global systems GPS, GLONASS, Galileo, and BeiDou and their respective satellite models (temporary satellite outages disregarded)

2.2 IGS products and analysis centers

The International GNSS Service (IGS) provides GNSS data and products of high quality for free use to the public. Established in 1994, its initial focus was on GPS, while GLONASS products were officially added in 2005, after some years of experimentation (Dow et al., 2009). In 2012, the Multi-GNSS Experiment (MGEX) was initiated as an answer to the changing landscape of GNSS (Montenbruck et al., 2014). The IGS collects GNSS observations from a global network of more than 400 permanent ground stations (see Figure 2.2) and redistributes them to a number of analysis centers. The analysis centers compute a variety of products, namely GPS and GLONASS orbits, GPS satellite and station clocks, station coordinates, Earth orientation parameters (EOPs), and some atmospheric parameters (Dow et al., 2009). The estimated EOPs comprise polar motion, polar motion rate, and length of day (LOD). Table 2.3 lists the current IGS orbit products. While the final orbit products offer the best quality, they are only provided with a delay of roughly two weeks. Therefore, a big focus in the recent past was the optimization of global data distribution to improve the latency of ultra-rapid products, which are intended for use in real time and near real time applications.

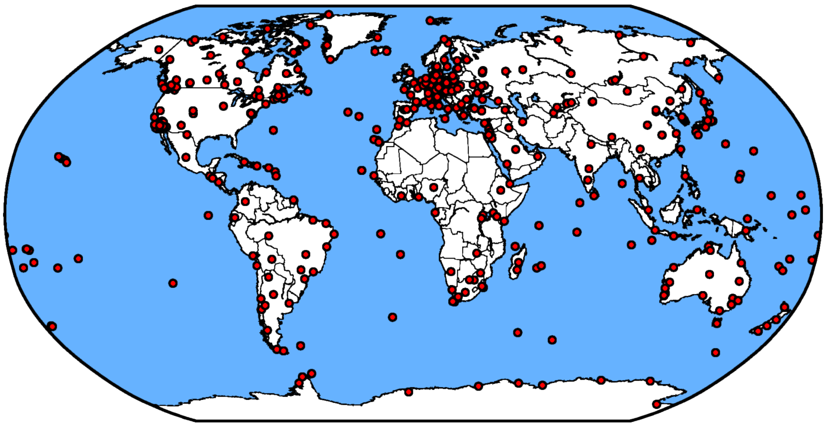

Fig. 2.2: Global network of over 400 IGS permanent stations

Tab. 2.3: IGS orbit products (Dow et al., 2009; Griffiths, 2013; International GNSS Service, 2016c)

Series	Product type	Accuracy	Latency
Ultra-rapid (predicted half)	GPS orbits GLONASS orbits GPS sat. clocks	~5 cm 1D RMS ~10 cm 1D RMS ~3 ns RMS, ~1.5 ns STD	Real time
Ultra-rapid (observed half)	GPS orbits GLONASS orbits GPS sat. clocks	~3 cm 1D RMS ~5 cm 1D RMS ~150 ps RMS, ~50 ps STD	3–9 hours
Rapid	GPS orbits GPS sat. clocks	~2.5 cm 1D RMS ~75 ps RMS, ~25 ps STD	17–41 hours
Final	GPS orbits GLONASS orbits GPS sat. clocks	<2.5 cm 1D RMS <5 cm 1D RMS ~75 ps RMS, ~20 ps STD	12–18 days

Twelve institutions are currently listed as official IGS analysis centers (see Table 2.4), although not all of them contribute to every product. While the overall quality and consistency of individual analysis center solutions have certainly improved over time, there are still differences in the computed orbits, as Figure 2.3 shows exemplarily. These differences can be attributed to some variation in the approaches, models, and software packages used by the individual analysis centers. During the combination process, this random-like noise is reduced, which generally results in a more robust and precise combined solution (Kouba, 2009). The orbit combination process was originally based on the L^1-norm and has since been greatly improved (Beutler et al., 1995; Springer et al., 1998).

Tab. 2.4: Current IGS analysis centers and utilized GNSS software (International GNSS Service, 2016b)

Institution	Abbrev.	Country	Software
Natural Resources Canada	EMR	Canada	GIPSY-OASIS
Wuhan University	WHU	China	PANDA
Geodetic Observatory Pecny	GOP	Czech Republic	Bernese
Groupe de Recherche de Géodésie Spatiale	GRGS	France	GINS/DYNAMO
GeoForschungsZentrum	GFZ	Germany	EPOS
European Space Operations Centre	ESA	Germany	NAPEOS
Center for Orbit Determination in Europe	CODE	Switzerland	Bernese
Jet Propulsion Laboratory	JPL	USA	GIPSY-OASIS
Massachusetts Institute of Technology	MIT	USA	GAMIT/GLOBK
National Geodetic Survey	NGS	USA	pages/gpscom
Scripps Institution of Oceanography	SIO	USA	GAMIT/GLOBK
U.S. Naval Observatory	USNO	USA	Bernese

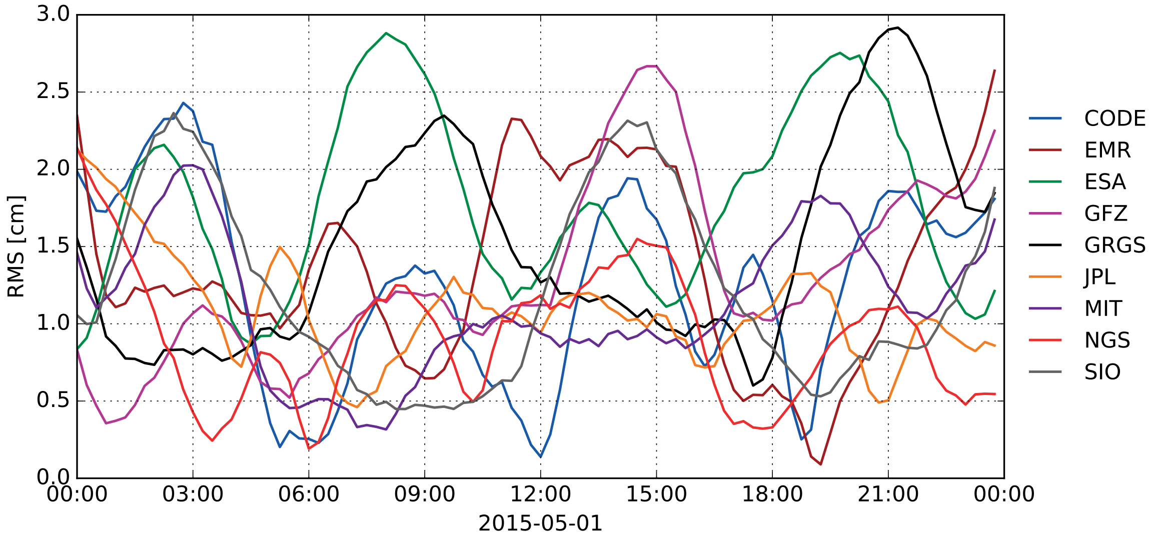

Fig. 2.3: Root mean square (RMS) of individual analysis center solutions compared to the combined IGS final orbit for GPS satellite G07 on 1 May 2015

Basics of GNSS orbit determination

3

Three different approaches have been established to determine precise satellite orbits using GNSS observation: kinematic, dynamic, and reduced-dynamic orbit determination. Kinematic orbit determination (Švehla and Rothacher, 2005; Zehentner and Mayer-Gürr, 2015) is not based on the equations of motion and does not require external force models. Instead, satellite positions are directly determined from the observations in each epoch. Therefore, the resulting time series of positions can be relatively noisy compared to other approaches. Kinematic orbits are highly sensitive to measurement errors and poor measurement geometry. Another issue is the possibility of data gaps. GNSS satellite orbits are in general not determined kinematically. However, this approach is commonly used in gravity field determination because it does not require an a priori gravity field model.

In contrast, dynamic orbit determination (e.g. Montenbruck and Gill, 2000) uses the equations of motion in combination with a priori physical models to describe a satellite orbit. The modeled orbit is then fitted to GNSS observations by estimating the initial state of the satellite via least squares adjustment. This results in a continuous orbit that is free of gaps, generally smooth and less prone to bad measurements. However, the precision of dynamic orbits is highly dependent on the quality of the physical models. For long arcs, e.g. 24 h as is common for GNSS orbits, small deficiencies in the force models accumulate during numerical integration. An insufficiently modeled orbit results in increased residuals when it is fitted to the observations.

The third approach, known as reduced-dynamic orbit determination (Jäggi, 2007; Swatschina, 2012), has been established to improve the fit of a modeled orbit to observations by introducing empirical parameters to the least squares adjustment. This approach is usually used for precise orbit determination of GNSS satellites, mostly due to deficiencies in the modeling of nonconservative forces. While these pseudo-stochastic parameters usually increase the orbit fit quality, they are not of physical origin and it is therefore generally preferable to strive for better models to improve dynamic orbit determination.

The following section briefly covers orbit modeling, that is the numerical integration of force models to compute a satellite orbit. The necessary force models to achieve an adequate modeling accuracy are described in the subsequent section. Another section focuses on variational equations. They are used to access the partial derivatives of a modeled orbit with respect to its initial state and dynamical parameters, e.g. solar radiation pressure parameters.

Using GNSS observation to determine satellite orbits requires linearization of the GNSS observation equations due to their nonlinear nature with respect to satellite positions. The modeled orbits are used as a priori reference orbits for linearization in the analyses conducted within the scope of this thesis. These orbits were fitted to IGS final orbits in a preprocessing step to obtain approximate values for the initial state vector and solar radiation pressure parameters, which are described in detail in Section 3.2.2. Linearization in combination with variational equations then enables a least squares fit of the modeled orbits to GNSS observations. During this adjustment, the initial state vector and solar radiation pressure parameters are updated. Furthermore, additional parameters related to the GNSS observation equations are estimated. These parameters are covered in Chapter 4 and include ionospheric and tropospheric parameters, clock errors, and more.

3.1 Orbit modeling

Orbit modeling is based on the equations of motion, a system of second-order differential equations that describe the motion of a satellite orbiting Earth. In the inertial frame the equation reads as

$$\ddot{\boldsymbol{r}}(t) = -\frac{GM}{r^3}\boldsymbol{r}(t) + \boldsymbol{a}(t, \boldsymbol{r}, \dot{\boldsymbol{r}}, p_1, ..., p_n) = \boldsymbol{f}(t, \boldsymbol{r}, ...) \ , \tag{3.1}$$

where $\boldsymbol{r}$ is the geocentric position of the satellite, r is the norm of $\boldsymbol{r}$, $\ddot{\boldsymbol{r}}$ is the acceleration of the satellite, G is the gravitational constant, and M is the mass of Earth. The acceleration $\boldsymbol{a}$ contains all gravitational and nongravitational perturbations and depends on the time t, the position $\boldsymbol{r}$ and velocity $\dot{\boldsymbol{r}}$ of the satellite, and a number of additional force model parameters $p_1, ..., p_n$ (Montenbruck and Gill, 2000). The additional parameters are either known a priori through force models or estimated in a least squares adjustment.

Six constants of integration are required for a particular solution of a three-dimensional second-order differential equation. The initial position $\boldsymbol{r}(t_0)$ and velocity $\dot{\boldsymbol{r}}(t_0)$ of the satellite, the so-called initial state vector, or alternatively six Keplerian elements are usually chosen as constants of integration (Beutler, 2005). If all of the additional parameters are known, the $6 + n_p$ parameters uniquely describe a satellite orbit that can then be computed by numerical integration starting from the initial epoch t_0. Various integration techniques have been developed to solve the differential equations numerically. Some of these integration techniques are described in detail by Montenbruck and Gill (2000) and Beutler (2005).

3.2 Force models

A satellite orbiting Earth is affected by a large number of forces, which can be divided into conservative and nonconservative forces, often also denoted as gravitational and nongravitational forces. Figure 3.1 gives an overview of the forces acting on a satellite orbiting Earth and their orders of magnitude.

Models for conservative forces are well established and generally offer sufficient quality for GNSS applications. Conservative forces include:

- Earth's gravity field
- Third-body attractions
- Solid Earth tides
- Ocean tides
- Pole tide
- Ocean pole tide
- Global mass variations
- Relativistic effects

Nonconservative forces are a key factor for precise orbit determination of GNSS satellites (Rodríguez Solano, 2014). Nonconservative forces relevant to GNSS satellites are:

- Solar radiation pressure
- Earth radiation pressure
- Antenna thrust

Due to their high altitude, GNSS satellites are not affected by atmospheric drag, which is the major nonconservative force acting on LEO satellites. Therefore, solar radiation pressure is the dominating nonconservative force relevant to GNSS satellites and currently a limiting factor for orbit accuracy. Inherent to solar radiation pressure is Earth radiation pressure, which consists of solar radiation reflected from Earth's surface, called Earth albedo, and thermal reradiation. A small but nonetheless important force to consider for GNSS satellites is antenna thrust, which is caused by signal transmission towards Earth.

In the case of reduced-dynamic orbits, empirical parameters are added in addition to the conservative and nonconservative force models. They do not represent any physical effects and are purely used to overcome deficiencies in the known force models.

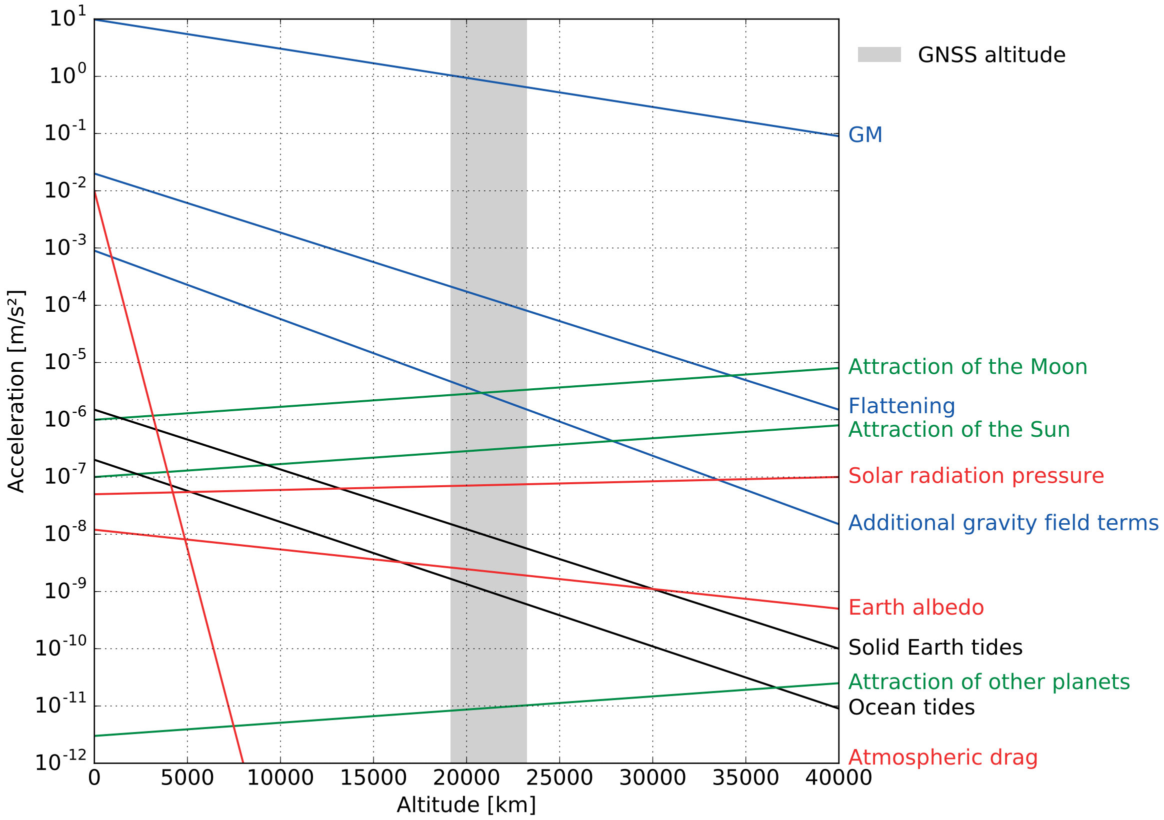

Fig. 3.1: Accelerations acting on a satellite orbiting Earth due to Earth's gravity field (blue), third-body attractions (green), tides (black), and nonconservative forces (red) (based on Montenbruck and Gill, 2000)

3.2.1 Conservative forces

The International Earth Rotation and Reference Systems Service (IERS) conventions (Petit and Luzum, 2010) offer detailed descriptions for modeling conservative forces, which are summarized in the following subsections.

3.2.1.1 Earth's gravity field

The static gravity field of Earth is often represented as an expansion of the gravitational potential V into a series of spherical harmonics (Hofmann-Wellenhof and Moritz, 2006)

$$V(r, \vartheta, \lambda) = \frac{GM}{R} \sum_{n=0}^{\infty} \left(\frac{R}{r}\right)^{n+1} \sum_{m=-n}^{n} a_{nm} Y_{nm}(\vartheta, \lambda) \,, \tag{3.2}$$

where r, ϑ, λ are spherical coordinates of the evaluation point, G is the gravitational constant, M is Earth's mass, and R is a constant reference radius. The basis functions

$$Y_{nm}(\vartheta, \lambda) = P_{nm}(\cos\vartheta) \begin{cases} \cos m\lambda & \text{if } m \geq 0 \\ \sin m\lambda & \text{otherwise} \end{cases} \tag{3.3}$$

are surface spherical harmonics using fully normalized Legendre functions $P_{nm}(\cos\vartheta)$ of the first kind of degree n and order m. The spherical-harmonic coefficients

$$a_{nm} = \begin{cases} c_{nm} & \text{if } m \geq 0 \\ s_{nm} & \text{otherwise} \end{cases} \tag{3.4}$$

are usually estimated using data from satellite gravity missions like Challenging Minisatellite Payload (CHAMP), Gravity Recovery And Climate Experiment (GRACE), and Gravity field and steady-state Ocean Circulation Explorer (GOCE). The coefficient $c_{00} = 1$ per definition, the first-degree coefficients $c_{10} = c_{11} = s_{11} = 0$ if the coordinate system origin is in the center of mass. The flattening of Earth is the main perturbation of the gravity field and is represented by the coefficient c_{20}. The remaining second-degree coefficients are related to polar motion and the ellipticity of the equator (Maier, 2015). In practice, the series of spherical harmonics in Equation (3.2) is limited to a maximum degree n_{max}, which is very low for GNSS satellites due to the attenuation of Earth's gravity field at high altitudes. The gravitational acceleration $\ddot{\boldsymbol{r}}_{\text{gf}}$ is the gradient vector of the gravitational potential

$$\ddot{\boldsymbol{r}}_{\text{gf}}(r, \vartheta, \lambda) = \nabla V(r, \vartheta, \lambda) \ , \tag{3.5}$$

which is obtained using the Nabla operator. Equation (3.5) has to be transformed from spherical to Cartesian coordinates and from the Earth-fixed system into the inertial system (Hofmann-Wellenhof and Moritz, 2006). High quality gravity field models are provided by the International Centre for Global Earth Models (ICGEM) (Barthelmes and Köhler, 2012).

3.2.1.2 Third-body attractions

Third-body attractions, often denoted as direct or astronomical tides, cause the second largest perturbation of a GNSS satellite orbit after the inhomogeneous part of Earth's gravity field. The main third bodies to consider are the Moon because of its close distance and the Sun because of its large mass. Attractions of other planets in our solar system are several orders of magnitude smaller, with Venus and Jupiter being the dominant contributors (Montenbruck and Gill, 2000). The acceleration $\ddot{\boldsymbol{r}}_{\text{tb}}$ due to a third body can be expressed as

$$\ddot{\boldsymbol{r}}_{\text{tb}} = GM_{\text{tb}} \left(\frac{\boldsymbol{r}_{\text{tb}} - \boldsymbol{r}}{\|\boldsymbol{r}_{\text{tb}} - \boldsymbol{r}\|^3} - \frac{\boldsymbol{r}_{\text{tb}}}{\|\boldsymbol{r}_{\text{tb}}\|^3} \right) \ , \tag{3.6}$$

where GM_{tb} is the gravitational parameter of the third body, $\boldsymbol{r}_{\text{tb}}$ is the geocentric position of the third body and $\boldsymbol{r}$ is the satellite's geocentric position. The second term within the parentheses of Equation (3.6) accounts for translative accelerations of Earth's center of mass due to third-body attractions (Tapley et al., 2004).

3.2.1.3 Solid Earth tides

Earth is a nonrigid body and therefore experiences mass redistribution and deformation of its surface due to external forces, namely the gravitational pull of the Moon and the Sun. This causes changes in the gravity field that in turn affect the forces acting on a satellite orbiting Earth. The changes of the gravitational potential induced by solid Earth tides are usually modeled as variations in the spherical-harmonic coefficients c_{nm} and s_{nm}. The variations Δc_{nm} and Δs_{nm} can be expressed in terms of Love numbers k_{nm}, which measure the elasticity of Earth. Furthermore, ellipsoidal corrections and frequency-dependent corrections are added to the Δc_{nm} and Δs_{nm} values. The IERS conventions (Petit and Luzum, 2010) provide more information about solid Earth tides along with nominal values for the Love numbers.

3.2.1.4 Ocean tides

Astronomical tides are not only responsible for solid Earth tides, they also cause mass redistribution in the oceans. Similar to solid Earth tides, ocean tides are usually incorporated as periodic variations of the spherical-harmonic coefficients c_{nm} and s_{nm}. The variations Δc_{nm} and Δs_{nm} can be computed from ocean tide models, which are typically provided as gridded maps of tide height amplitudes for selected main tidal frequencies. Examples for widely used ocean tide models are FES2004 (Lyard et al., 2006) and EOT11a (Savcenko and Bosch, 2012). Further details on ocean tide models and their implementation can be found in the IERS conventions (Petit and Luzum, 2010). The influence of ocean tides on GNSS satellite orbits is an order of magnitude smaller than that of solid Earth tides.

3.2.1.5 Pole tide

The centrifugal effect of polar motion generates the (solid Earth) pole tide, which causes a perturbation in the external potential. This perturbation is equivalent to changes in the spherical-harmonic coefficients c_{21} and s_{21}. The changes in the coefficents

$$\Delta c_{21} = -1.333 \cdot 10^{-9} \, (m_1 + 0.0115 \, m_2) \tag{3.7}$$

$$\Delta s_{21} = -1.333 \cdot 10^{-9} \, (m_2 - 0.0115 \, m_1) \tag{3.8}$$

depend on the wobble variables m_1, m_2 (in arcseconds). These variables are given by

$$m_1 = x_p - \bar{x}_p \quad \text{and} \quad m_2 = -(y_p - \bar{y}_p) \, , \tag{3.9}$$

where x_p, y_p are the polar motion variables and $\bar{x}_p, \bar{y}_p$ are their running averages. More details are provided in the IERS conventions (Petit and Luzum, 2010).

3.2.1.6 Ocean pole tide

Similar to the pole tide, the centrifugal effect of polar motion on the oceans generates the ocean pole tide. Polar motion is dominated by the Chandler wobble and annual variations. The displaced ocean surface is expected to be in equilibrium with the forcing equipotential surface at such long periods (Petit and Luzum, 2010). A self-consistent equilibrium model of the ocean pole tide, which accounts for continental boundaries, mass conservation in the oceans, self-gravitation, and loading of the ocean floor, is provided by Desai (2002). The ocean pole tide can be expressed by variations in the spherical-harmonic coefficients c_{nm} and s_{nm}. The dominant coefficient variations are given by

$$\Delta c_{21} = -2.1778 \cdot 10^{-10} \, (m_1 + 0.01724 \, m_2) \tag{3.10}$$

$$\Delta s_{21} = -1.7232 \cdot 10^{-10} \, (m_2 - 0.03365 \, m_1) \tag{3.11}$$

and depend on the wobble variables m_1, m_2 (in arcseconds), see Equation (3.9). The second-degree coefficients constitute approximately 90% of the ocean pole tide's variance, followed by the first-degree and third-degree coefficients, respectively. Approximately 99% of the variance is covered by expansion up to degree $n = 10$. The IERS conventions (Petit and Luzum, 2010) provide further details on the computation of the coefficients for the full model.

3.2.1.7 Global mass variations

Global high-frequency mass variations due to nontidal atmospheric pressure variations, wind-induced ocean currents, and changes in terrestrial water storage lead to small variations in Earth's gravity field. These mass variations can therefore influence satellite orbits, although this influence is significantly smaller than that of the main tidal forces, e.g. solid Earth tides or ocean tides. Global mass variations are usually deduced from a combination of atmospheric models and ocean models. The former model atmospheric pressure, temperature, and moisture and the latter are used to obtain ocean bottom pressure values (Dobslaw et al., 2013).

A widely used model for global atmospheric and oceanic mass variations is the Atmosphere and Ocean De-aliasing Level 1B (AOD1B) product in its current release 05 version (Dobslaw et al., 2013). This model was created to reduce aliasing effects in monthly GRACE gravity fields. It is provided as a series of spherical-harmonic coefficients up to degree and order 100 with a 6-hour sampling that can be added to the coefficients of the static gravity field.

3.2.1.8 General relativity

Orbit determination of near-Earth satellites has to account for general relativity by correcting the equations of motion, the time transformations, and the measurement models. For orbit modeling, the relativistic correction to the acceleration of a satellite orbiting Earth is given in the Geocentric Celestial Reference System (GCRS) by

$$
\begin{aligned}
\ddot{\boldsymbol{r}}_{\text{rel}} = {} & \frac{GM_E}{c^2 r^3}\left\{\left[2(\beta+\gamma)\frac{GM_E}{r} - \gamma\,\dot{\boldsymbol{r}}\cdot\dot{\boldsymbol{r}}\right]\boldsymbol{r} + 2(1+\gamma)(\boldsymbol{r}\cdot\dot{\boldsymbol{r}})\dot{\boldsymbol{r}}\right\} \\
& + (1+\gamma)\frac{GM_E}{c^2 r^3}\left[\frac{3}{r^2}(\boldsymbol{r}\times\dot{\boldsymbol{r}})(\boldsymbol{r}\cdot\boldsymbol{J}) + (\dot{\boldsymbol{r}}\times\boldsymbol{J})\right] \\
& + \left\{(1+2\gamma)\left[\dot{\boldsymbol{R}}\times\left(\frac{-GM_S\boldsymbol{R}}{c^2 R^3}\right)\right]\times\dot{\boldsymbol{r}}\right\} ,
\end{aligned}
\tag{3.12}
$$

where c is the speed of light, β and γ are parameterized post-Newtonian (PPN) parameters, equal to 1 in general relativity, $\boldsymbol{r}$ is the geocentric satellite position, $\boldsymbol{R}$ is the position of Earth with respect to the Sun, $\boldsymbol{J}$ is Earth's angular momentum per unit mass ($|\boldsymbol{J}| \cong 9.8 \cdot 10^8\,\mathrm{m}^2/\mathrm{s}$), and GM_E and GM_S are the gravitational coefficients of Earth and the Sun, respectively.

The Schwarzschild field of Earth, covered by the first line of Equation (3.12), describes the main relativistic effects on a satellite orbiting Earth and leads to a shift in the argument of perigee (Ashby and Bertotti, 1986). In comparison to the main Newtonian accelerations, the Schwarzschild terms are smaller by a factor of 10^9 for low orbits to 10^{10} for high orbits. The Lense-Thirring effect, also known as frame-dragging and covered by the second line, and the geodesic (de Sitter) precession, covered by the third line, cause a precession of the orbital plane. Both of these effects are about 10^{11} to 10^{12} times smaller than the main Newtonian accelerations. Further details can be found in the IERS conventions (Petit and Luzum, 2010).

3.2.2 Nonconservative forces

The effects of nonconservative forces on GNSS satellite orbits are small compared to the main conservative forces. While conservative forces can be modeled very well, modeling of nonconservative forces is still a major challenge. Solar radiation pressure in particular is the largest error source of GNSS orbit determination (Springer et al., 1999).

The following subsections provide details on direct solar radiation pressure, indirect solar radiation pressure due to Earth albedo and thermal reradiation, and antenna thrust. Atmospheric drag is not covered since it does not affect GNSS satellites because of their high altitude.

3.2.2.1 Solar radiation pressure

When a satellite is exposed to solar radiation, it experiences a small force due to the absorption and reflection of photons. The acceleration caused by solar radiation depends on the satellite's mass, attitude, surface area, and surface properties. A detailed derivation of the acceleration acting on a satellite due to solar radiation pressure is given by Montenbruck and Gill (2000), starting from the solar flux and concluding in

$$\ddot{\boldsymbol{r}}_{\text{srp}} = -P_S \left(\frac{1\,\text{AU}}{r_S}\right)^2 \frac{A}{m} \cos\vartheta \left[(1-\epsilon)\boldsymbol{e}_S + 2\,\epsilon \cos\vartheta\, \boldsymbol{n}\right] , \tag{3.13}$$

where P_S is the solar radiation pressure at a distance of one astronomical unit (AU) from the Sun ($P_S \approx 4.56 \cdot 10^{-6}\,\text{N}/\text{m}^2$), r_S is the distance between the satellite and the Sun, A is the surface area, m is the satellite's mass, ϵ is the reflectivity coefficient of the satellite component (typically ranging from 0.2 to 0.9 depending on the material), $\boldsymbol{e}_S$ is the unit vector from the satellite to the Sun, $\boldsymbol{n}$ is the unit normal vector of the surface, and

$$\cos\vartheta = \boldsymbol{n}^T \cdot \boldsymbol{e}_S \; . \tag{3.14}$$

Since GNSS satellites have a complex shape and structure and are composed of a large variety of surface materials, simplified box-wing models are often used in orbit determination. In these macro models, only the main surfaces are modeled to reduce the computational effort and complexity of the model. Another consideration that has to be made is the fact that surface properties are measured on ground prior to launch and may not represent real in-orbit behavior of a satellite, e.g. due to aging materials or uncertainty of the a priori properties (Rodríguez Solano, 2014). Nonetheless, the first solar radiation pressure models were based on physical properties and have been developed and used for the GPS satellite blocks I, II, IIA, and IIR (Fliegel et al., 1992; Fliegel and Gallini, 1996).

The drawbacks of physically-based solar radiation pressure models resulted in research into models that are empirically derived from the actual behavior of in-orbit satellites. Empirical models directly account for the combined effect of solar radiation pressure on all satellite components. These models are tunable and adjustable and therefore get more accurate with longer time series of real orbit data (Springer et al., 1999; Bar-Sever and Kuang, 2004). Unfortunately, empirically-derived a priori solar radiation pressure models are not sufficiently accurate for precise orbit determination on the level of IGS final orbit products. Therefore, it is necessary to estimate solar radiation pressure parameters during orbit determination. A model used by many IGS analysis centers is the empirical CODE orbit model (ECOM) developed by the Center for Orbit Determination in Europe (Beutler et al., 1994; Springer et al., 1999). The model consists of up to nine empirical parameters and reads as

$$\ddot{\boldsymbol{r}}_{\text{srp}} = \ddot{\boldsymbol{r}}_{0,\text{srp}} + D(u)\,\boldsymbol{e}_D + Y(u)\,\boldsymbol{e}_Y + B(u)\,\boldsymbol{e}_B \; , \tag{3.15}$$

with $\ddot{\boldsymbol{r}}_{0,\text{srp}} = \boldsymbol{0}$ if no a priori solar radiation pressure model is used and

$$\begin{aligned} D(u) &= D_0 + D_C \cos u + D_S \sin u \\ Y(u) &= Y_0 \ + Y_C \ \cos u + Y_S \ \sin u \\ B(u) &= B_0 + B_C \cos u + B_S \sin u \ . \end{aligned} \tag{3.16}$$

Here, u is the argument of latitude of the satellite, the parameters D_0, Y_0, B_0 are direct terms and $D_C, D_S, Y_C, Y_S, B_C, B_S$ are once-per-revolution terms. The parameters are estimated in a coordinate frame with axes D, Y, and B, where D points from the satellite towards the Sun, Y points along the satellite's solar panel axis and B completes the right-handed system. The two most widely used variations of this model estimate either five parameters (D_0, Y_0, B_0, B_C, B_S), subsequently called ECOM5, or all nine parameters, subsequently denoted as ECOM9. A recent update to the model (Arnold et al., 2015) recommends to add two-per-revolution and four-per-revolution terms for the D-axis to the ECOM5 variation. Additionally, the angular argument is changed to the difference between the argument of latitude of the satellite and of the Sun, $\Delta u = u_{\text{Sat}} - u_{\text{Sun}}$. This results in a new variation of the ECOM with nine parameters that reads as

$$\begin{aligned} D(\Delta u) &= D_0 + D_{C2} \cos 2\Delta u + D_{S2} \sin 2\Delta u + D_{C4} \cos 4\Delta u + D_{S4} \sin 4\Delta u \\ Y(\Delta u) &= Y_0 \\ B(\Delta u) &= B_0 + B_C \cos \Delta u + B_S \sin \Delta u \ , \end{aligned} \tag{3.17}$$

which will subsequently be denoted as ECOM9N. The mentioned three variations ECOM5, ECOM9, and ECOM9N are the primary solar radiation pressure models used in the numerical analyses of this thesis. Research has also been conducted on combined physical and empirical models, e.g. an adjustable box-wing model (Rodríguez Solano, 2014). In practice, the IGS analysis centers do not use a priori solar radiation pressure models in their routine orbit determination process and instead estimate empirical parameters.

Another aspect of modeling solar radiation pressure that has to be considered is Earth shadowing. A satellite in Earth's shadow is not affected by any direct solar radiation pressure. GNSS satellites experience a so-called eclipse season during which they enter Earth's shadow once per revolution. The frequency and duration of shadow crossings depend on the satellite orbit parameters and the constellation of Earth and the Sun. For example, GPS satellites experience two eclipse season per year that last about 30–40 days, depending on the orbital plane (Fliegel et al., 1992). Shadow crossings of GPS satellites can last from a few minutes at the beginning of an eclipse season to almost an hour at its peak. Earth shadowing is usually accounted for by using either cylindrical models or conical models that also include partial shadow (penumbra). Montenbruck and Gill (2000) provide a detailed description of a penumbra model, which results in a scaling factor that is one if a satellite is outside Earth's shadow and zero if it is within full shadow (umbra). In penumbra the factor depends on the visible part of the Sun.

3.2.2.2 Earth radiation pressure

Solar radiation affects satellites not only directly but also indirectly in the form of Earth radiation. Earth radiation is divided into a reflective part, called Earth albedo, and an emissive part, known as thermal reradiation. While reflection only occurs on the illuminated parts of Earth, thermal radiation is emitted on the parts of Earth that are in shadow as well. Rodríguez Solano (2009) developed a model for Earth radiation pressure that is now widely used for GNSS orbit determination by IGS analysis centers. It is based on a box-wing satellite model and uses global reflection and emission data provided by the National Aeronautics and Space Administration (NASA) experiment Clouds and the Earth's Radiant Energy System (CERES), see Wielicki et al. (1996).

3.2.2.3 Antenna thrust

GNSS satellites transmit a number of signals towards Earth, which results in a small constant radial acceleration away from Earth. The acceleration due to antenna thrust is given by

$$\ddot{\boldsymbol{r}}_{\text{at}} = -\frac{P}{mc}\boldsymbol{e}_z \ , \tag{3.18}$$

where P is the antenna transmit power, m is the satellite's mass, c is the speed of light, and $\boldsymbol{e}_z$ is the unit vector pointing along the antenna towards Earth (Rodríguez Solano, 2009). IGS model values for antenna transmit power are 76 W for GPS I, II, and IIA, 85 W for GPS IIR, 198 W for GPS IIR-M, and 249 W for GPS IIF (International GNSS Service, 2016a). As there are no official values for other GNSS, assumptions have to be made to model antenna thrust, e.g. 100 W for GLONASS II and M satellites.

3.2.3 Empirical parameters

The fit of a modeled orbit to observations can be improved by augmenting the orbit model with empirical parameters. They are used to overcome imperfections in the force models that can add up during numerical integration. This is especially relevant to GNSS orbit determination due to commonly long arcs, e.g. 24 h for many IGS analysis centers. Empirical parameters are also often referred to as pseudo-stochastic parameters since a priori stochastic properties and constraints are usually assigned to them. The most common occurrence of empirical parameters in GNSS orbit determination are instantaneous velocity changes, also known as pseudo-stochastic pulses, that are usually applied once in the center of a 24 h arc (Beutler et al., 1994). Empirical parameters are described in more detail by Jäggi (2007), including additional modeling techniques. It has to be noted that empirical parameters do not represent any physical effect and therefore improved modeling of conservative and nonconservative forces is preferable for physically realistic orbit determination.

3.3 Variational equations

Montenbruck and Gill (2000) and Beutler (2005) provide very detailed explanations of variational equations, which are summarized in this section. Fitting a dynamic orbit to observations requires the partial derivatives of the equations of motion with respect to the initial state $\boldsymbol{r}_0, \dot{\boldsymbol{r}}_0$ and dynamical parameters $\boldsymbol{p} = \{p_1, ..., p_m\}$. In the case of GNSS orbit determination, the dynamical parameters usually comprise solar radiation pressure parameters and potentially pseudo-stochastic pulses. For satellite gravity missions the dynamical parameters would include the spherical-harmonic coefficients c_{nm} and s_{nm}.

Using the state vector and its time derivative,

$$\boldsymbol{y}(t) = \begin{pmatrix} \boldsymbol{r}(t) \\ \dot{\boldsymbol{r}}(t) \end{pmatrix} \qquad \text{and} \qquad \dot{\boldsymbol{y}}(t) = \begin{pmatrix} \dot{\boldsymbol{r}}(t) \\ \boldsymbol{f}(t, \boldsymbol{r}, ...) \end{pmatrix} , \tag{3.19}$$

the equations of motion can be written as a system of six first-order differential equations

$$\dot{\boldsymbol{y}}(t) = \bar{\boldsymbol{f}}(t, \boldsymbol{y}, ...) \, . \tag{3.20}$$

Derivating Equation (3.20) with respect to the initial state vector $\boldsymbol{y}_0 = (\boldsymbol{r}_0 \;\; \dot{\boldsymbol{r}}_0)^T$ gives

$$\frac{\partial \dot{\boldsymbol{y}}(t)}{\partial \boldsymbol{y}_0} = \underbrace{\frac{\partial \bar{\boldsymbol{f}}(t, \boldsymbol{y}, ...)}{\partial \boldsymbol{y}_0}}_{=\boldsymbol{0}} + \frac{\partial \bar{\boldsymbol{f}}(t, \boldsymbol{y}, ...)}{\partial \boldsymbol{y}} \frac{\partial \boldsymbol{y}(t)}{\partial \boldsymbol{y}_0} , \tag{3.21}$$

which can also be written as

$$\dot{\boldsymbol{\Phi}}(t) = \frac{\partial \bar{\boldsymbol{f}}(t, \boldsymbol{y}, ...)}{\partial \boldsymbol{y}} \boldsymbol{\Phi}(t) \qquad \text{with} \qquad \boldsymbol{\Phi}(t)_{6\times 6} = \frac{\partial \boldsymbol{y}(t)}{\partial \boldsymbol{y}_0} \tag{3.22}$$

or

$$\dot{\boldsymbol{\Phi}}(t) = \begin{bmatrix} \boldsymbol{0}_{3\times 3} & \mathbf{I}_{3\times 3} \\ \dfrac{\partial \boldsymbol{f}(t, \boldsymbol{r}, ...)}{\partial \boldsymbol{r}(t)} & \boldsymbol{0}_{3\times 3} \end{bmatrix}_{6\times 6} \boldsymbol{\Phi}(t) \, . \tag{3.23}$$

The state transition matrix $\boldsymbol{\Phi}$ represents the partial derivatives of a satellite's position and velocity with respect to the initial state vector $\boldsymbol{y}_0$ and is computed by numerical integration of Equation (3.22) starting from the initial value $\boldsymbol{\Phi}_0 = \mathbf{I}_{6\times 6}$. Similar to Equation (3.21), derivation of Equation (3.20) with respect to the dynamical parameters $\boldsymbol{p}$ gives

$$\frac{\partial \dot{\boldsymbol{y}}(t)}{\partial \boldsymbol{p}} = \frac{\partial \bar{\boldsymbol{f}}(t, \boldsymbol{y}, ...)}{\partial \boldsymbol{p}} + \frac{\partial \bar{\boldsymbol{f}}(t, \boldsymbol{y}, ...)}{\partial \boldsymbol{y}} \frac{\partial \boldsymbol{y}(t)}{\partial \boldsymbol{p}} , \tag{3.24}$$

which can be rephrased to

$$\dot{\mathbf{S}}(t) = \frac{\partial \bar{\boldsymbol{f}}(t, \boldsymbol{y}, ...)}{\partial \boldsymbol{p}} + \frac{\partial \bar{\boldsymbol{f}}(t, \boldsymbol{y}, ...)}{\partial \boldsymbol{y}} \mathbf{S}(t) \qquad \text{with} \qquad \mathbf{S}(t)_{6\times m} = \frac{\partial \boldsymbol{y}(t)}{\partial \boldsymbol{p}} \tag{3.25}$$

or

$$\dot{\mathbf{S}}(t) = \begin{bmatrix} \mathbf{0}_{3\times m} \\ \dfrac{\partial \boldsymbol{f}(t, \boldsymbol{r}, ...)}{\partial \boldsymbol{p}} \end{bmatrix}_{6\times m} + \begin{bmatrix} \mathbf{0}_{3\times 3} & \mathbf{I}_{3\times 3} \\ \dfrac{\partial \boldsymbol{f}(t, \boldsymbol{r}, ...)}{\partial \boldsymbol{r}(t)} & \mathbf{0}_{3\times 3} \end{bmatrix}_{6\times 6} \mathbf{S}(t) \ . \tag{3.26}$$

Here, the partial derivatives of a satellite's position and velocity with respect to the dynamical parameters $\boldsymbol{p}$ are contained in the parameter sensitivity matrix $\mathbf{S}$. This matrix can be computed by numerical integration starting from the initial value $\mathbf{S}_0 = \mathbf{0}_{6\times m}$, since the initial state vector does not depend on any dynamical parameter. Alternatively, the parameter sensitivity matrix can be computed directly from the state transition matrix by solving

$$\mathbf{S}(t) = -\boldsymbol{\Phi}(t) \int_{t_0}^{t} \boldsymbol{\Phi}^{-1}(t') \begin{bmatrix} \mathbf{0}_{3\times m} \\ \dfrac{\partial \boldsymbol{f}(t', \boldsymbol{r}, ...)}{\partial \boldsymbol{p}} \end{bmatrix}_{6\times m} dt' \ . \tag{3.27}$$

Once the state transition matrix $\boldsymbol{\Phi}$ and the parameter sensitivity matrix $\mathbf{S}$ are computed for every epoch, the partial derivatives of the orbit with respect to the initial state $\boldsymbol{y}_0$ and dynamical parameters $\boldsymbol{p}$ are known. The partial derivatives of a GNSS observation equation $\rho(t)$ with respect to the initial state or dynamical parameters can then be formed using the chain rule, e.g.

$$\frac{\partial \rho(t)}{\partial \boldsymbol{y}_0} = \frac{\partial \rho(t)}{\partial \boldsymbol{y}(t)} \frac{\partial \boldsymbol{y}(t)}{\partial \boldsymbol{y}_0} = \frac{\partial \rho(t)}{\partial \boldsymbol{y}(t)} \boldsymbol{\Phi}(t) \tag{3.28}$$

or

$$\frac{\partial \rho(t)}{\partial \boldsymbol{p}} = \frac{\partial \rho(t)}{\partial \boldsymbol{y}(t)} \frac{\partial \boldsymbol{y}(t)}{\partial \boldsymbol{p}} = \frac{\partial \rho(t)}{\partial \boldsymbol{y}(t)} \mathbf{S}(t) \ . \tag{3.29}$$

The partial derivative of an observation equation with respect to the current state $\boldsymbol{y}(t)$ that appears in Equations (3.28) and (3.29) is straightforward to compute. With observation equations linked to the initial state and dynamical parameters, the orbit can then be fitted to GNSS observations in an iterative least squares adjustment. The subsequent chapter will cover the observation equations used in the raw observation approach.

The raw observation approach

4

The raw observation approach is a new GNSS processing method presented by Zehentner and Mayer-Gürr (2014) and Zehentner and Mayer-Gürr (2015) in the context of kinematic orbit determination of LEO satellites. One of the main goals of this thesis was the adaption of this approach to precise orbit determination of GNSS satellites. Therefore, this chapter is largely based on these two publications. The approach is based on four basic principles:

- Directly use all available observations.
- Do not form linear combinations or observation differences.
- Correct all known influences in advance.
- Estimate remaining influences as additional parameters.

According to the first principle, all available code and phase observations are directly used in one least squares adjustment. Most of the methods that are currently used for high-precision GNSS processing rely on the ionosphere-free linear combination to reduce the first-order ionospheric influence. Observation differences are also often used to reduce several additional errors. The most common observation difference is the so-called double-difference, because it eliminates both satellite and receiver clock biases and allows to directly access integer ambiguities (Hofmann-Wellenhof et al., 2008). Inherent drawbacks of linear combinations and differences are increased measurement noise and the reduction of the number of available observations. As the second principle indicates, the raw observation approach does not use linear combinations or observation differences and therefore all observations and their original accuracy levels are maintained. Consequently, all systematic influences must either be known in advance or estimated as parameters in the least squares adjustment, as stated by the third and fourth principles.

The influences that have to be considered either as a priori corrections or as parameters to be estimated in the least squares adjustment include:

- Transmitter orbit
- Transmitter clock error
- Transmitter antenna characteristics
- Phase wind-up
- Relativistic effects

- Space-time curvature
- Code biases
- Phase biases
- Phase ambiguities
- Ionospheric refraction
- Tropospheric refraction
- Receiver position
- Receiver clock error
- Receiver antenna characteristics
- Multipath and signal diffraction

This list makes it clear that the sought-after transmitter orbit is just one out of many different components that must be taken into account. Estimating unknown influences in the least squares adjustment is both a drawback and an advantage. Increasing the number of estimated parameters reduces the redundancy, but at the same time it gives the possibility to directly access and analyze various constituents. As an example, the ambiguities associated with each phase observation are estimated individually, which facilitates detailed investigation of each ambiguity. Avoiding observation combinations also makes incorporating new observables rather straightforward. This is especially important in view of the significant expansion of available GNSS observables that is currently happening, e.g. with the introduction of GPS L5 or new systems like Galileo and BeiDou. New observables introduce new combinations and thus new correlations due to the mixing of different errors and parameters. Treating all observations separately allows to also access all errors and parameters separately. Furthermore, the parametrization of a single component may be changed without affecting the composition of other parameters.

4.1 Basic observation equations

Following Hofmann-Wellenhof et al. (2008), the basic observation equations for code and phase measurements between satellite s and receiver r are

$$R = \rho + c\,\delta_r - c\,\delta^s \tag{4.1}$$

and

$$\lambda\,\Phi = \rho + c\,\delta_r - c\,\delta^s + \lambda\,n\ , \tag{4.2}$$

where R is the code measurement and Φ is the phase measurement. The range ρ between satellite and receiver contains the unknown receiver position and in the case of orbit determination also the unknown satellite position. The satellite and receiver clock errors, δ^s and δ_r, are both unknown in the case of orbit determination, with c being the speed of light. For phase observations, the unknown number of cycles n, called ambiguity, has to be considered as well. The wavelength λ depends on the carrier frequency, however this is not denoted explicitly in this chapter for the sake of simplicity.

GNSS measurements are affected by several further influences that have to be considered in addition to the basic set of parameters mentioned above. Some of these influences are well known and can be modeled sufficiently. Therefore, they can be directly reduced from the observations. Other influences must be either known in advance, e.g. by using code biases determined by the Center for Orbit Determination in Europe (CODE), or estimated as additional parameters in the least squares adjustment. The following section details corrections and additional parameters that have to be considered for precise orbit determination.

4.2 Corrections and additional parameters

4.2.1 Antenna corrections

Satellite and receiver antenna corrections are provided by the IGS in the so-called antenna exchange (ANTEX) format. Detailed information on this format along with definitions of the uniform axis convention used by the IGS can be found in Montenbruck et al. (2015). Satellite antenna corrections include the main offset along the z-axis towards Earth and potential offsets along the x- and y-axis, depending on the satellite model. These offsets relate the satellite's antenna position to its center of mass position. For receiver antennas, the IGS provides information on eccentricity and orientation in the so-called solution independent exchange (SINEX) format. The main eccentricity for receiver antennas is the height offset.

In addition to offsets, antenna center variations are also provided for both satellites and receivers. GNSS code and phase measurements are related to the electronic center of the antenna, which is not a physically defined point. The electronic center depends on the antenna type, carrier frequency, observation type, signal direction (azimuth and elevation), and the surroundings of the antenna, which may cause multipath effects. All observations are related to a common point, which is defined by a mean antenna center, and deviate by azimuth- and elevation-dependent variations. For satellite antennas, the IGS definition of these variations depends purely on the nadir angle and the satellite model. Zehentner and Mayer-Gürr (2015) showed that satellite antenna center variations also depend on the azimuth and a nadir-only representation is not sufficient. Further investigations are necessary to determine how this affects precise orbit determination of GNSS satellites. IGS receiver antenna center variations are determined by robot calibrations and depend on both azimuth and elevation.

4.2.2 Phase wind-up, relativistic effects, and space-time curvature

Radio waves transmitted by GNSS satellites are right circularly polarized. Therefore, the carrier phase measured by a receiver depends on the mutual orientation of the satellite and receiver antennas. Rotations of the satellite or receiver antenna around their respective bore axis (z-axis for satellite and up-axis for receiver antennas) result in changes of up to one cycle in the carrier phase. This effect, called phase wind-up, is further described by Kouba (2009).

The motion of a satellite and the gravitational potential difference between satellite and receiver position influence the nominal frequency of the satellite clock. The corresponding effects of special and general relativity on the satellite clock can be expressed as

$$\Delta_{\text{rel}} = -\frac{2}{c^2}\boldsymbol{r}^s \cdot \dot{\boldsymbol{r}}^s \ , \tag{4.3}$$

where Δ_{rel} is in seconds, c is the speed of light, and $\boldsymbol{r}^s$ and $\dot{\boldsymbol{r}}^s$ are the satellite's position and velocity vectors (Hofmann-Wellenhof et al., 2008).

The satellite signal is also affected by space-time curvature caused by the gravitational field. Following Hofmann-Wellenhof et al. (2008), the corresponding range correction is

$$\Delta_{\text{stc}} = \frac{2\,GM}{c^2} \ln \frac{r^s + r_r + \rho_r^s}{r^s + r_r - \rho_r^s} \ , \tag{4.4}$$

where Δ_{stc} is in meters, GM is Earth's gravitational parameter, c is the speed of light, r^s and r_r are the geocentric distances of the satellite and receiver, and ρ_r^s is the range between them.

4.2.3 Code biases

In addition to the civil C1C code, geodetic GNSS receivers also measure code observables like C1P, C2P, or a combination C1C $+$ (C2P $-$ C1P), denoted as C2D in the receiver independent exchange (RINEX) version 3.03 format (International GNSS Service, 2015). Common receiver classes are:

- C1P/C2P (C1C code data is usually disregarded)
- C1C/C2D (called cross-correlation receivers)
- C1C/C2P

C1C, C1P, and C2P measurements contain instrumental biases $(B_{\text{C1C}}, B_{\text{C1P}}, B_{\text{C2P}})$ that are not accessible in an absolute sense. For this reason, they are considered as differences

$$B_{\text{C1P}-\text{C2P}} = B_{\text{C1P}} - B_{\text{C2P}} \tag{4.5}$$

$$B_{\text{C1P}-\text{C1C}} = B_{\text{C1P}} - B_{\text{C1C}} \ , \tag{4.6}$$

which are called differential code biases. In large GNSS station networks with receivers from multiple classes it is necessary to correct C1C/C2D and C1C/C2P receivers in order to achieve consistency with C1P/C2P receivers, for which the correction is zero by convention if the ionosphere-free linear combination is used. In case of the approach used in this thesis, corrections have to be applied to the raw L1 and L2 code observations according to Table 4.1. An extended description of differential code biases can be found in Dach et al. (2007). Monthly differential code bias solutions for each GPS satellite are provided, for instance, by the Center for Orbit Determination in Europe.

Tab. 4.1: Code bias corrections for L1 and L2 code observations due to satellite-specific differential code bias values $B_{\mathrm{C1P-C2P}}$ and $B_{\mathrm{C1P-C1C}}$. f_{L1} and f_{L2} are the respective carrier frequencies for L1 and L2 (Dach et al., 2007).

Receiver	**L1 code bias correction**	**L2 code bias correction**
C1P/C2P	$\frac{f_{\mathrm{L2}}^2}{f_{\mathrm{L1}}^2 - f_{\mathrm{L2}}^2} B_{\mathrm{C1P-C2P}}$	$\frac{f_{\mathrm{L1}}^2}{f_{\mathrm{L1}}^2 - f_{\mathrm{L2}}^2} B_{\mathrm{C1P-C2P}}$
C1C/C2D	$\frac{f_{\mathrm{L2}}^2}{f_{\mathrm{L1}}^2 - f_{\mathrm{L2}}^2} B_{\mathrm{C1P-C2P}} + B_{\mathrm{C1P-C1C}}$	$\frac{f_{\mathrm{L1}}^2}{f_{\mathrm{L1}}^2 - f_{\mathrm{L2}}^2} B_{\mathrm{C1P-C2P}} + B_{\mathrm{C1P-C1C}}$
C1C/C2P	$\frac{f_{\mathrm{L2}}^2}{f_{\mathrm{L1}}^2 - f_{\mathrm{L2}}^2} B_{\mathrm{C1P-C2P}} + B_{\mathrm{C1P-C1C}}$	$\frac{f_{\mathrm{L1}}^2}{f_{\mathrm{L1}}^2 - f_{\mathrm{L2}}^2} B_{\mathrm{C1P-C2P}}$

4.2.4 Phase ambiguities and phase biases

If GNSS phase observations are utilized, it is necessary to consider the associated unknown number of cycles, called phase ambiguities. In practice, it is not possible to directly estimate the integer part of the phase ambiguities in the least squares adjustment. Therefore, the initial solution of estimated phase ambiguities is usually called float solution. In order to achieve highest accuracies in terms of positioning error, it is essential to resolve the phase ambiguities and fix them to integer values. Depending on the observation type, different ambiguity resolution techniques such as the classic double-differenced approach (e.g. Hofmann-Wellenhof et al., 2008) or, more recently, various undifferenced or zero-difference approaches are used (Ge et al., 2008; Geng et al., 2010; Loyer et al., 2012). Undifferenced ambiguity resolution requires explicit modeling or estimation of all the influences that are eliminated with the double-difference approach. This means the unknown float parts at both the satellite and receiver, which are caused by internal hardware delays, have to be determined since they are not eliminated (Ge et al., 2008). Shi (2012) and Shi and Gao (2014) compare a variety of different methods that have been proposed to handle these phase biases. However, ambiguity resolution is not a focus of this thesis.

4.2.5 Ionospheric influence

The ionosphere is a dispersive medium with respect to GNSS radio frequency bands. This results in delayed code measurements, which travel at group velocity, and advanced phase measurements, which travel at phase velocity. The ionosphere-free linear combination (e.g. Hofmann-Wellenhof et al., 2008) is commonly used to eliminate the ionospheric influence. Alternatively, the ionospheric influence can be accounted for by estimating the total electron content (TEC) along the signal path. This additional parameter, denoted as the slant TEC (STEC), can be added to the basic observation equations for code and phase observations given in Equations (4.1) and (4.2), which then read as

$$R = \rho + c\,\delta_r - c\,\delta^s + \left(\Delta I_{\text{gr}}^{(1)} + \Delta I_{\text{gr}}^{(2)} + \Delta I_{\text{gr}}^{(3)}\right) STEC \tag{4.7}$$

and

$$\lambda\,\Phi = \rho + c\,\delta_r - c\,\delta^s + \lambda\,n + \left(\Delta I_{\text{ph}}^{(1)} + \Delta I_{\text{ph}}^{(2)} + \Delta I_{\text{ph}}^{(3)}\right) STEC\ . \tag{4.8}$$

Here, the superscript denotes the order of the correction term. While the first-order term covers approximately 99 % of the ionospheric influence, Fritsche et al. (2005) showed that it is necessary to include second- and third-order terms to achieve centimeter or even millimeter accuracy. For code observations, the three terms as given by Fritsche et al. (2005) are

$$\Delta I_{\text{gr}}^{(1)} = \frac{40.3}{f^2} \tag{4.9}$$

$$\Delta I_{\text{gr}}^{(2)} = \frac{7527c}{f^3}(\boldsymbol{B}_0 \cdot \boldsymbol{k}) \tag{4.10}$$

$$\Delta I_{\text{gr}}^{(3)} = \frac{2437}{f^4} N_{\text{max}}\,\eta \tag{4.11}$$

and for phase observations, they are

$$\Delta I_{\text{ph}}^{(1)} = -\Delta I_{\text{gr}}^{(1)} \tag{4.12}$$

$$\Delta I_{\text{ph}}^{(2)} = -\frac{1}{2}\Delta I_{\text{gr}}^{(2)} \tag{4.13}$$

$$\Delta I_{\text{ph}}^{(3)} = -\frac{1}{3}\Delta I_{\text{gr}}^{(3)}\ . \tag{4.14}$$

Equations (4.9) to (4.14) depend on the carrier frequency f, the speed of light c, the magnetic field vector $\boldsymbol{B}_0$, the signal propagation unit vector $\boldsymbol{k}$, the peak electron density N_{max}, and a shape parameter η. A value for the shape parameter ($\eta = 0.66$) and an approximation formula for N_{max} are given by Fritsche et al. (2005). The magnetic field vector $\boldsymbol{B}_0$ can be obtained by using the International Geomagnetic Reference Field (IGRF) (Thebault et al., 2015), which is provided by the International Association of Geomagnetism and Aeronomy (IAGA).

In addition to being delayed or advanced, a GNSS signal is also bent on its way through the ionosphere due to the varying refractive index along the path between satellite and receiver. This means the signal travels along a curved instead of a straight path between satellite and receiver and therefore the corresponding distance is measured too long. Hoque and Jakowski (2008) refer to this as the bending effect and provide an empirical correction formula

$$\Delta I_{\text{bending}} = \frac{7.5 \cdot 10^{-5}\, STEC^2\, e^{-2.13\,\beta}}{f^4\, HF_2\, (h_m F_2)^{0.125}} \ , \tag{4.15}$$

where $\Delta I_{\text{bending}}$ is in meters, $STEC$ is in TEC units (1 TEC unit = 10^{16} electrons/m^2), β is the elevation angle in radians, f is the carrier frequency in GHz, HF_2 is the F_2 layer scale height in kilometers, and $h_m F_2$ is the peak ionization height in kilometers.

Due to the dispersive nature of the ionosphere, the curved signal path also slightly differs depending on the carrier frequency of the GNSS signal. Therefore, the signals represent different STEC values, which is referred to as TEC difference range error by Hoque and Jakowski (2008). The empirical correction formula for this error is

$$\Delta I_{\Delta\text{TEC}} = \frac{40.3}{f^2}\, \frac{0.1108\, STEC^2\, e^{-2.1844\,\beta}}{f^2\, HF_2\, (h_m F_2)^{0.3}} \ , \tag{4.16}$$

where $\Delta I_{\Delta\text{TEC}}$ is converted from electrons/m^2 to meters via the first term on the right side, $STEC$ is in electrons/m^2, β is in radians, HF_2 and $h_m F_2$ are in kilometers, and f is in Hertz. Global mean values can be used for the peak ionization height $h_m F_2$ and the layer scale height HF_2 in Equations (4.15) and (4.16). $STEC$ is estimated as a parameter in the least squares adjustment. The corrections from Equations (4.15) and (4.16) can be directly applied to the observations.

4.2.6 Tropospheric influence

The IERS conventions (Petit and Luzum, 2010) provide a detailed description of tropospheric modeling for radio techniques, which is summarized in this section. The troposphere is a nondispersive medium with respect to GNSS signals and imposes a delay of up to a few meters depending on the path of the signal through the troposphere. This delay is commonly divided into a hydrostatic and a wet component. The hydrostatic component accounts for roughly 80–100 % of the total delay, depending on the site location and time of year. While the hydrostatic component can be accurately computed a priori, the same is not the case for the wet component. For precise GNSS applications it is therefore necessary to additionally estimate the residual wet delay. The tropospheric line-of-sight delay ΔT is expressed as a function of four parameters and reads as

$$\Delta T = m_{\text{h}}(e) D_{\text{zh}} + m_{\text{w}}(e) D_{\text{zw}} + m_{\text{g}}(e) \left[G_{\text{N}} \cos a + G_{\text{E}} \sin a \right] \ , \tag{4.17}$$

where the four parameters are the zenith hydrostatic delay D_{zh}, the zenith wet delay D_{zw}, and a horizontal delay gradient with components G_{N} and G_{E}, with a being the azimuth angle. Horizontal gradient parameters account for a systematic component in the north-south direction and also capture random effects due to weather systems. They are usually estimated as additional parameters in precise GNSS applications if observations below 15° elevation are utilized (Petit and Luzum, 2010). The hydrostatic, wet, and gradient mapping functions m_{h}, m_{w}, and m_{g} all depend on the elevation angle e and are given by

$$m_{\text{h,w}}(e) = \frac{1 + \cfrac{a}{1 + \cfrac{b}{1 + c}}}{\sin e + \cfrac{a}{\sin e + \cfrac{b}{\sin e + c}}} \tag{4.18}$$

and

$$m_{\text{g}}(e) = \frac{1}{\sin e \tan e + 0.0032} \ . \tag{4.19}$$

The coefficients a, b, and c for Equation (4.18) and a priori zenith hydrostatic and wet delays D_{zh} and D_{zw} are provided by global troposphere models like the Vienna Mapping Functions 1 (VMF1) (Boehm et al., 2006). Adding the tropospheric delay to the basic observation equations given in Equations (4.1) and (4.2) results in

$$R - \Delta T_{\text{ap}} = \rho + c\,\delta_r - c\,\delta^s + m_{\text{w}}(e)\Delta D_{\text{zw}} + m_{\text{g}}(e)\left[G_{\text{N}}\cos a + G_{\text{E}}\sin a\right] \tag{4.20}$$

for code observations and

$$\lambda\,\Phi - \Delta T_{\text{ap}} = \rho + c\,\delta_r - c\,\delta^s + \lambda\,n + m_{\text{w}}(e)\Delta D_{\text{zw}} + m_{\text{g}}(e)\left[G_{\text{N}}\cos a + G_{\text{E}}\sin a\right] \tag{4.21}$$

for phase observations, where ΔT_{ap} is the a priori tropospheric correction and ΔD_{zw}, G_{N}, and G_{E} are the additional parameters to be estimated in the least squares adjustment.

4.2.7 Station displacements

GNSS stations are affected by displacements due to various effects that are detailed in Chapter 7 of the IERS conventions (Petit and Luzum, 2010). These displacements relate the instantaneous position of a station to its regularized position, which excludes these higher frequency effects. In the case of the global IGS station network, regularized station positions are provided in the form of weekly SINEX files containing station coordinates and velocities. Conventional models for displacements include the effects of solid Earth tides, ocean tidal loading, atmospheric pressure loading, rotational deformation due to polar motion (pole tide), and ocean pole tide loading. Some of these effects are also briefly described in Section 3.2.1 of this thesis with respect to orbit modeling.

Since station coordinates usually refer to the International Terrestrial Reference System (ITRS) and satellite orbits to the International Celestial Reference System (ICRS), reference system rotations have to be accounted for as well. The IERS conventions (Petit and Luzum, 2010) extensively describe the realization of both systems and the transformation between them. Some IGS analysis centers routinely estimate Earth orientation parameters (EOPs) related to this transformation. EOPs that can be derived from GNSS observations include polar motion, polar motion rate, and length of day (LOD).

4.3 Extended observation equations

Extending the basic observation equations given in Equations (4.1) and (4.2) by the additional parameters for the ionosphere and troposphere and correcting them for known influences finally leads to

$$\begin{aligned} R - \Delta R = \rho + c\,\delta_r - c\,\delta^s + \left(\Delta I^{(1)}_{\text{gr}} + \Delta I^{(2)}_{\text{gr}} + \Delta I^{(3)}_{\text{gr}}\right) STEC \\ + m_{\text{w}}(e)\Delta D_{\text{zw}} + m_{\text{g}}(e)\left[G_{\text{N}}\cos a + G_{\text{E}}\sin a\right] \end{aligned} \tag{4.22}$$

for code observations and

$$\begin{aligned} \lambda\,\Phi - \Delta\Phi = \rho + c\,\delta_r - c\,\delta^s + \lambda\,n + \left(\Delta I^{(1)}_{\text{ph}} + \Delta I^{(2)}_{\text{ph}} + \Delta I^{(3)}_{\text{ph}}\right) STEC \\ + m_{\text{w}}(e)\Delta D_{\text{zw}} + m_{\text{g}}(e)\left[G_{\text{N}}\cos a + G_{\text{E}}\sin a\right] \end{aligned} \tag{4.23}$$

for phase observations. The corrections ΔR and $\Delta\Phi$ contain all known influences that can be corrected a priori for the respective observation type. These influences have been detailed in the previous section and include antenna offsets and antenna center variations, phase wind-up, relativistic effects, space-time curvature, differential code biases, bending correction, TEC difference range correction, tropospheric corrections, and station displacements. The parameters to be estimated in the least squares adjustment are the receiver and satellite clock errors, δ_r and δ^s, the slant TEC value $STEC$, the tropospheric zenith wet delay residual ΔD_{zw}, and tropospheric horizontal gradient components G_{N} and G_{E}. In case of phase observations, the unknown ambiguities n have to be estimated as well. Further parameters to be estimated are station positions and satellite orbits, which are both implicitly contained in the range ρ.

Based on the extended observation equations, the least squares adjustment can be set up. Using both code and phase observations in one least squares adjustment requires a realistic weighting scheme due to the different measurement accuracies. Common practice in GNSS processing is to use elevation-dependent observation weights. This means an a priori standard deviation for each observation type is scaled with respect to the elevation angle. Variance component estimation (Koch and Kusche, 2002) can then be used to estimate the relative weighting of different observation groups from observation residuals and redundancies. This method also accounts for possible outliers by continuously reducing their weight with each iteration until they practically do not contribute to the parameter estimation anymore. Depending on the estimated parameters, it might be necessary to add constraints to the least squares adjustment to avoid datum defects. Possible constraints comprise pseudo-observations, no-net-rotations, or no-net-translations (Petit and Luzum, 2010). As an example, if both satellite orbits and station positions are estimated, the whole system can be freely rotated in space without changing the relative observations within the system. This datum defect can be solved by applying a no-net-rotation constraint to the satellite orbits or station positions, which means the mean rotation of all satellite orbits or station positions is constrained to zero.

5

Numerical analyses of the effects of force models on GNSS orbit modeling

Chapter 3 lists the various forces that affect GNSS satellite orbits and details how they can be modeled. This chapter presents results of numerical analyses to illustrate the effect of these models on GPS orbits. The analyses conducted in this chapter focus solely on orbit modeling, that is the numerical integration of force models. In contrast to orbit determination, which is discussed in Chapter 6, this means the results presented in this chapter are not based on GPS observations. The analyzed time period covers nine years from the beginning of 2007 to the end of 2015. For each day in this time period, a 24-hour orbit arc with a 5-minute sampling was modeled for every operational GPS satellite. The corresponding IGS final orbits acted as reference orbits. Utilizing the reference orbits as pseudo-observations, the modeled orbits were fitted to the reference orbits in a least squares sense by estimating the initial state vector and solar radiation pressure parameters as detailed in Chapter 3.

The following analyses were carried out with respect to conservative forces:

- Difference due to gravity field model selection
- Influence of ocean tides
- Difference due to ocean tide model selection
- Influence of global mass variations
- Influence of pole tide
- Influence of ocean pole tide

Conducted analyses of the effect of nonconservative forces on orbit modeling include:

- Difference due to solar radiation pressure model selection
- Influence of Earth radiation pressure
- Influence of antenna thrust

Table 5.1 lists the force models that were used as reference settings for the analysis scenarios listed above. For each scenario, the investigated model was then either disabled or, if the difference between models was of interest, replaced by an alternative model. The differences between orbits modeled with the reference settings and with scenario-specific settings were used to determine the influence of the investigated model on GPS orbits. In the case of

Tab. 5.1: Force models used as reference settings for the analysis scenarios

Effect	Model	Reference
Gravity field	GOCO05s	Mayer-Gürr et al. (2015)
Third-body attractions	JPL DE421	Folkner et al. (2009)
Solid Earth tides	IERS 2010	Petit and Luzum (2010)
Ocean tides	EOT11a	Savcenko and Bosch (2012)
Global mass variations	AOD1B RL05	Dobslaw et al. (2013)
Pole tide	IERS 2010	Petit and Luzum (2010)
Ocean pole tide	IERS 2010	Petit and Luzum (2010)
General relativity	IERS 2010	Petit and Luzum (2010)
Solar radiation pressure	ECOM9N	Arnold et al. (2015)
Earth radiation pressure	Box-wing	Rodríguez Solano (2009)
Antenna thrust	IGS model values	International GNSS Service (2016a)

comparing different models for the same force, the results were used to determine if the selection of a specific model affects GPS orbits or if the only important aspect is that the force is modeled at all. Due to the large amount of orbit data, the root mean square (RMS) is utilized in the comparisons. Daily component-wise RMS values are computed via

$$\mathrm{RMS} = \sqrt{\frac{1}{3N}\sum_{i=1}^{N}\left\|\boldsymbol{r}_i - \boldsymbol{r}_i^{\mathrm{ref}}\right\|^2} = \sqrt{\frac{1}{3N}\sum_{i=1}^{N}\left(\Delta x_i^2 + \Delta y_i^2 + \Delta z_i^2\right)}\ , \tag{5.1}$$

either per satellite or as an overall RMS value combining all operational satellites.

5.1 Conservative forces

Figure 5.1 provides an overview of the results of all investigated analysis scenarios with respect to conservative forces. The daily overall RMS values for the influences of global mass variations, pole tide, and ocean pole tide are well below 1 mm and therefore these models may be omitted. With a daily overall RMS of around 2 mm, ocean tides have the largest influence of the investigated conservative forces. Looking at the comparison of the two models Empirical Ocean Tide model 2011a (EOT11a) (Savcenko and Bosch, 2012) and Finite Element Solution 2004 (FES2004) (Lyard et al., 2006), it does not seem to matter which ocean tide model is used, as long as it models the main tidal frequencies and is somewhat current.

One of the analysis scenarios related to conservative forces compares the gravity field models Gravity Observation Combination 05s (GOCO05s) (Mayer-Gürr et al., 2015) and Earth Gravitational Model 2008 (EGM2008) (Pavlis et al., 2012). The former was released in 2015 and combines GRACE and GOCE data, kinematic orbits, and satellite laser ranging (SLR) observations. The latter was released in 2008, contains both satellite and terrestrial data and is currently the recommended model for IGS analysis center processing. Only the very low degrees up to a maximum of $n = 12$ are relevant to GNSS satellites because of their high altitude.

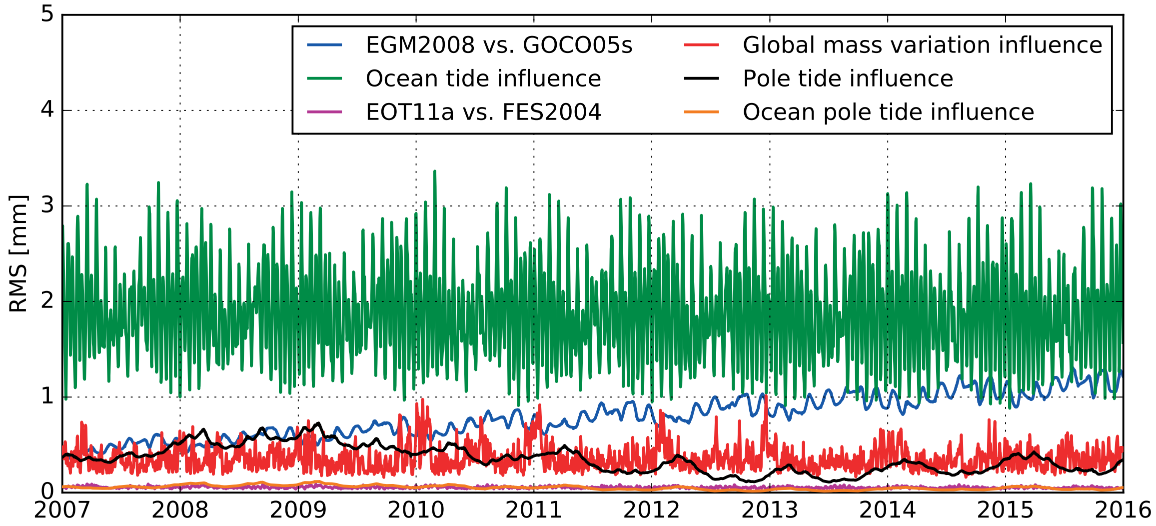

Fig. 5.1: Daily overall RMS values of analysis scenarios related to conservative forces. The influences of global mass variations (red), pole tide (black), and ocean pole tide (orange) are well below 1 mm and therefore negligible. While the influence of the ocean tide (green) is around 2 mm, there is no significant difference between the investigated ocean tide models EOT11a and FES2004 (magenta). The difference between the gravity field models EGM2008 and GOCO05s (blue) shows a small trend caused by the inclusion of a temporal component in GOCO05s compared to the static-only EGM2008.

In this range, GOCO05s has superior accuracy because it includes a significantly longer time series of satellite data. GOCO05s also features a time-variable component consisting of a trend and an annual variation. This trend is clearly visible in Figure 5.1 because it is modeled in GOCO05s but not in EGM2008, which only features a static gravity field. While the difference is negligible at the beginning of the investigated time period, the overall RMS begins to exceed 1 mm in 2014. Therefore, it becomes increasingly important to use an up-to-date gravity field model like GOCO05s in GNSS orbit modeling.

5.2 Nonconservative forces

An overview of the analysis scenario results concerning nonconservative forces is given in Figure 5.2. With RMS values of around 3 mm, the influence of antenna thrust is the smallest investigated nonconservative force affecting GNSS satellites. Its influence still mostly exceeds that of ocean tides, which is the largest investigated conservative force. Furthermore, the influence of antenna thrust shows a small upward trend. This trend is caused by the modernization of the GPS constellation, where block IIR-M and IIF now constitute the majority of satellites. The transmission power of satellite blocks IIR-M (198 W) and IIF (249 W) is significantly larger than that of IIA (76 W) and IIR (85 W). The influence of Earth radiation pressure amounts for RMS values of around 8 mm and therefore definitely has to be accounted for in GNSS orbit modeling. The utilized box-wing model by Rodríguez Solano (2009) still seems to be the most sophisticated model for Earth radiation pressure and is widely used by

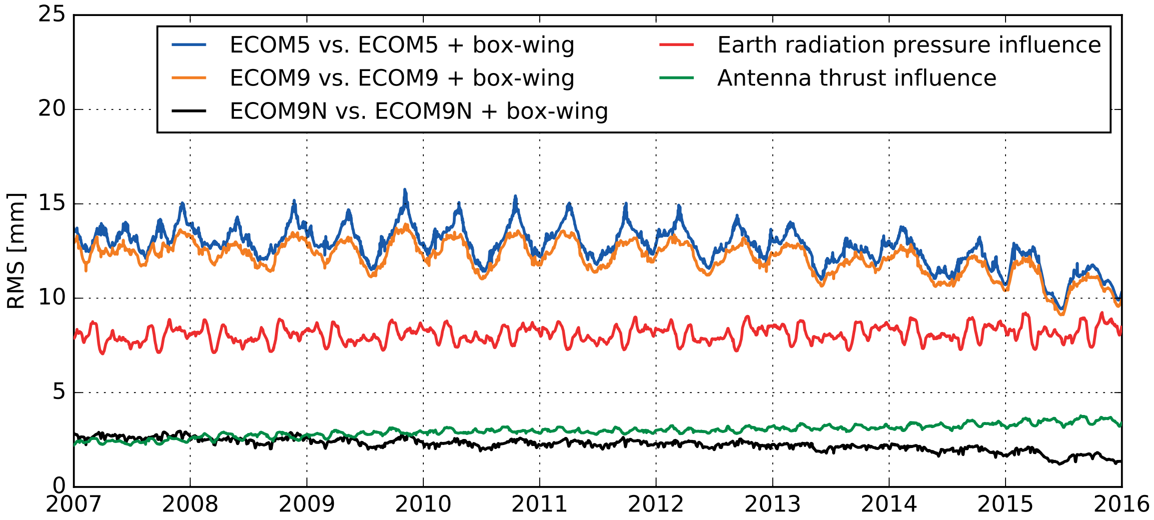

Fig. 5.2: Daily overall RMS values of analysis scenarios related to nonconservative forces. The comparison of the solar radiation pressure models ECOM5 (blue) and ECOM9 (orange) with and without an a priori box-wing model shows RMS values of around 13 mm and 12 mm. In contrast, the same comparison using ECOM9N (black) results in RMS values of 2 mm. This shows that the empirical model ECOM9N manages to capture most effects of the physical box-wing model, which is not the case for ECOM5 and ECOM9. With RMS values of around 8 mm, Earth radiation pressure (red) is a significant effect that has to be accounted for. The RMS values of antenna thrust influence (green) are around 3 mm and show a small upward trend due to an increasing number of modern satellites with higher transmission power.

IGS analysis centers in their processing. The box-wing model was additionally adapted for use as an a priori direct solar radiation pressure model to allow for further investigations. Numerical analyses showed that using only the adapted a priori box-wing model for direct solar radiation pressure modeling without estimating any additional terms is not a viable option at this point in time due to insufficient modeling accuracy. Nonetheless, this physical model can be assumed as a general approximation of the effects acting on a GPS satellite and therefore provides valuable information when compared to the commonly used empirical solar radiation pressure models, e.g. the empirical CODE orbit model (ECOM). Based on this, the analysis scenarios related to direct solar radiation pressure focused on whether the investigated empirical models are able to sufficiently capture these physical effects.

The investigated variations of the ECOM include ECOM5, ECOM9, and ECOM9N, which are detailed in Chapter 3. ECOM5 includes one direct term per axis and and two one-per revolution terms along the B-axis $(D_0, Y_0, B_0, B_C, B_S)$. ECOM9 comprises of one direct and two one-per-revolution terms per axis $(D_0, Y_0, B_0, D_C, D_S, Y_C, Y_S, B_C, B_S)$. ECOM9N features two two-per-revolution and two four-per-revolution terms along the D-axis in addition to the parameters of ECOM5 $(D_0, Y_0, B_0, B_C, B_S, D_{C2}, D_{S2}, D_{C4}, D_{S4})$. As Figure 5.2 shows, the daily overall RMS values of the comparisons between orbits modeled with and without the a priori box-wing model are around 13 mm for ECOM5, 12 mm for ECOM9, and 2 mm for ECOM9N. The fact that ECOM9N results in significantly lower RMS values indicates that the box-wing model includes two-per-revolution and/or four-per-revolution effects which are

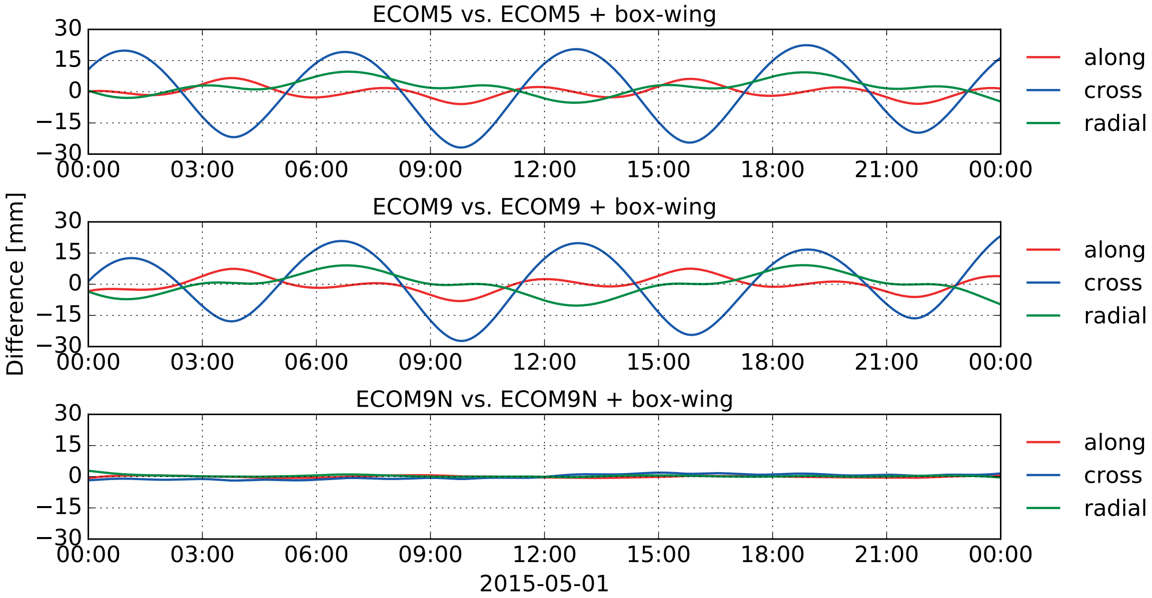

Fig. 5.3: Difference between orbits of GPS satellite G01 on 2015-05-01 modeled with and without an a priori box-wing model in addition to the ECOM5 (top), ECOM9 (center), and ECOM9N (bottom) solar radiation pressure models. ECOM5 and ECOM9 are unable to account for significant two-per-revolution effects that are modeled by the physical box-wing model. Using ECOM9N, the differences are severely reduced because ECOM9N includes additional two-per-revolution terms compared to ECOM5 and ECOM9.

not properly accounted for by ECOM5 and ECOM9. Looking at the orbit differences of a specific satellite on a single day as shown in Figure 5.3 confirms this indication. While both ECOM5 and ECOM9 clearly show orbit differences with a two-per-revolution frequency, these differences are severely reduced if ECOM9N is used. These results demonstrate that ECOM9N is able to model the effects of solar radiation pressure more realistically. Furthermore, it indicates that using ECOM5 or ECOM9 without an a priori model, which is common practice among some IGS analysis centers, may lead to insufficiencies in the modeled orbits. The conducted analyses regarding direct solar radiation pressure support the recommendation of the Center for Orbit Determination in Europe (Arnold et al., 2015) to use the new ECOM9N variation instead of ECOM5 or ECOM9.

6

Numerical analyses of precise orbit determination using real data

This chapter presents numerical analyses and results of precise orbit determination with the raw observation approach. All analyses were conducted using real data, e.g. observation data from the global IGS permanent station network and reference data including IGS final orbits, clocks, and station coordinates. While the concepts detailed in Chapters 3 and 4 apply to GNSS in general, the analyses were focused on GPS. This decision was made to reduce the complexity of the initial implementation, since this is the first time the raw observation approach has been used to determine orbits of GNSS satellites. The additional intricacy of system-specific characteristics and inter-system dependencies and correlations could therefore be avoided or reduced to a minimum. Moreover, GPS provides a long and robust time series of available data under full operational capability. It was further decided to limit the analyses to code and phase observations on the L1 and L2 frequency bands to ensure consistent conditions over the analyzed time period. The orbits were determined in terms of daily 24-hour arcs over a time period of nine years, from the beginning of 2007 to the end of 2015.

In the following section the modeled orbits, which were used as reference orbits for linearization, are analyzed in detail. These orbits were subsequently fitted to GPS observations during orbit determination. Section 6.2 focuses on the data, models, and settings that were used to determine GPS satellite orbits over the investigated time period. Finally, orbit determination results are presented, analyzed, and validated against orbits of specific IGS analysis centers and the combined IGS final orbits in Section 6.3.

6.1 Analysis of modeled orbits

The modeled orbits that were used as reference orbits for linearization are based on the force models listed in Table 5.1 on page 31. As mentioned in Chapter 3, the modeled orbits were fitted to IGS final orbits in a preprocessing step to get approximate values for the initial state vector and solar radiation pressure parameters. Figure 6.1 shows weekly RMS values of the modeled orbits in comparison to the IGS final orbits they were fitted to. With RMS values mostly below 1.5 cm, the modeled orbits generally fit well to the IGS final orbits in the analyzed time period. A noticeable pattern of increased RMS values over 30–40 days with a repetition rate of around six months correlates directly with the eclipse seasons of the respective satellites. Eclipse seasons are the periods where the constellation of a satellite's orbital plane, Earth and

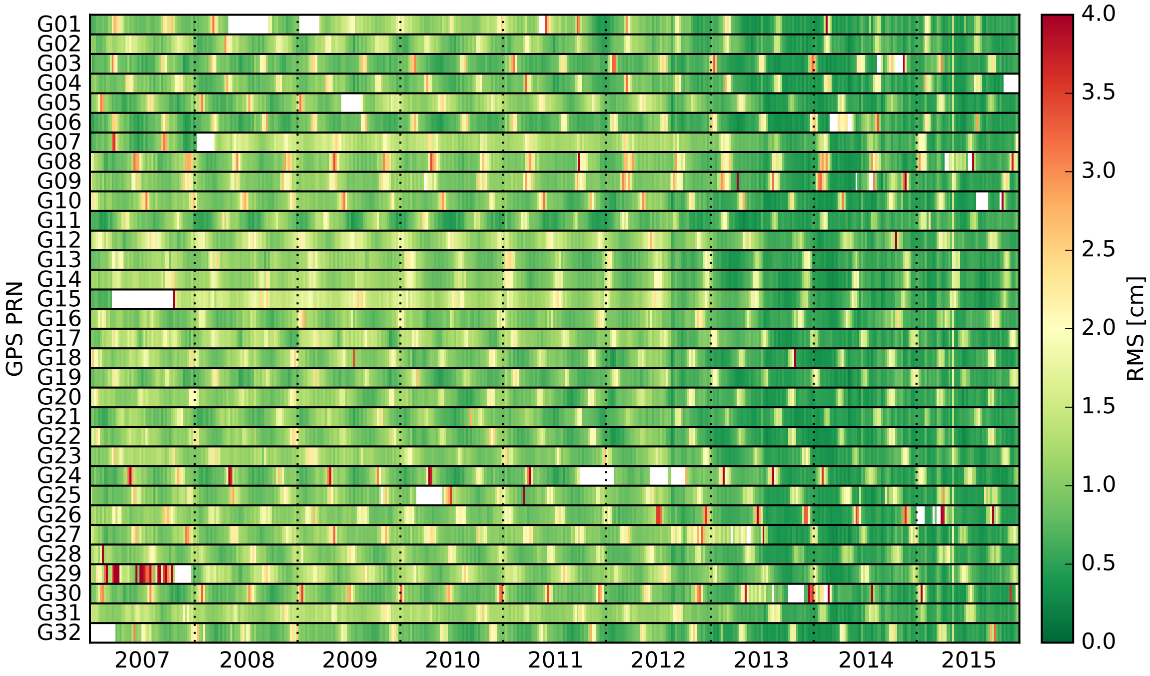

Fig. 6.1: Weekly RMS values of modeled orbits with 300 s sampling compared to IGS final orbits over the full analysis period. Green color represents a good fit of the modeled orbit to the reference IGS orbits, while yellow and red colors indicate discrepancies. A pattern of increased RMS values for 30–40 days occurring roughly every six months is clearly noticeable. This pattern correlates with the eclipse seasons of the respective satellites, identified by their pseudo-random noise (PRN) code from G01 to G32, and indicates deficiencies in orbit modeling during these periods.

the Sun makes a once-per-revolution shadow crossing of a satellite possible. The increased RMS values during eclipse seasons indicate deficiencies of orbit modeling for these periods. These deficiencies are related to solar radiation pressure modeling during eclipse season in combination with the initially utilized sampling of 300 s. The relatively abrupt change of solar radiation pressure at shadow entry and exit is insufficiently accounted for during numerical integration with the sampling chosen initially. As an example, if a satellite enters Earth's shadow a few seconds after an integration epoch, the acceleration due to solar radiation pressure is incorrectly applied for a period of almost five minutes until it is disabled at the next integration epoch. The same issue occurs at the beginning and end of an eclipse season, where shadow crossings only last a few minutes and therefore may disappear altogether during integration.

These issues can be mitigated through use of a smaller sampling during numerical integration, as Figure 6.2 shows exemplary for the first eclipse season of GPS satellite G01 in 2013. During eclipse season, the modeled orbit fits significantly better to the reference IGS final orbit if a smaller sampling of 120 s or 60 s is used. With these samplings, the RMS values within the eclipse season are on the same level as those outside eclipse season, where no difference between the analyzed sampling rates is visible at all. This indicates that the remaining deviation to the reference orbit is not caused by the selection of the sampling

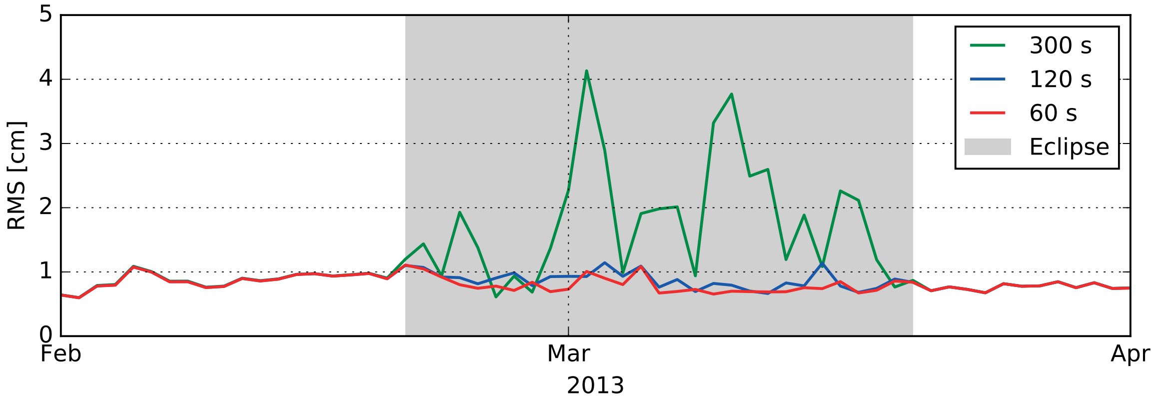

Fig. 6.2: Daily RMS values of modeled orbits using different samplings for GPS satellite G01 around its first eclipse season in 2013. Outside eclipse season (gray area), a smaller sampling has no effect on the modeled orbit compared to the 300 s (green) sampling initially used in the analyses. During eclipse season, using a smaller sampling of 120 s (blue) or 60 s (red) significantly improves the fit of the modeled orbit to the IGS final orbit. An even smaller sampling, e.g. 30 s, resulted in no further improvement.

rate. An even smaller sampling of 30 s resulted in no further improvement of the fit, which supports the aforementioned conclusion. Based on the findings above, the complete time series was recomputed with a sampling of 60 s. As Figure 6.3 shows, this resulted in a significant improvement of the RMS values during eclipse season for all but block IIA satellites. The issues with block IIA satellites stem from their unreliable behavior during and after their shadow crossings (Rodríguez Solano et al., 2013). In these periods, the attitude of block IIA satellites significantly deviates from their nominal attitude, which was used in the conducted analyses. These deviations directly affect the modeling of solar radiation pressure, Earth radiation pressure, and antenna thrust. Realistic attitude modeling during shadow crossings might therefore further improve the modeled orbits and has to be investigated in the future. From late 2012 onwards, the RMS values generally improve for all satellites, which aligns with and therefore may be related to the introduction of the IGb08 reference frame on 7 October 2012 (Dach and Jean, 2013).

The effect of using a 60 s sampling instead of 300 s is also visible in the estimated solar radiation pressure parameters, which are shown in Figure 6.4 for GPS satellite G01 in 2013. Both show deviations during eclipse seasons, but with 60 s the estimates are significantly more stable and deviate less from those outside eclipse season. In theory, if solar radiation pressure modeling during eclipse seasons was perfect, the estimated parameters should not deviate much from those outside eclipse season. This leads to the conclusion that a sampling of 60 s definitely benefits solar radiation pressure modeling during eclipse seasons and therefore improves the modeled orbits. Generally, the direct term D_0 is by far the largest term of the ECOM9N. It shows a clear correlation to the distance between the Sun and the satellite/Earth. The acceleration due to the direct term is at its peak at perihelion in early January, where Earth and therefore the satellite is closest to the Sun. It then slowly lowers as Earth approaches aphelion in early July, where it is farthest from the Sun, and then rises again. The acceleration

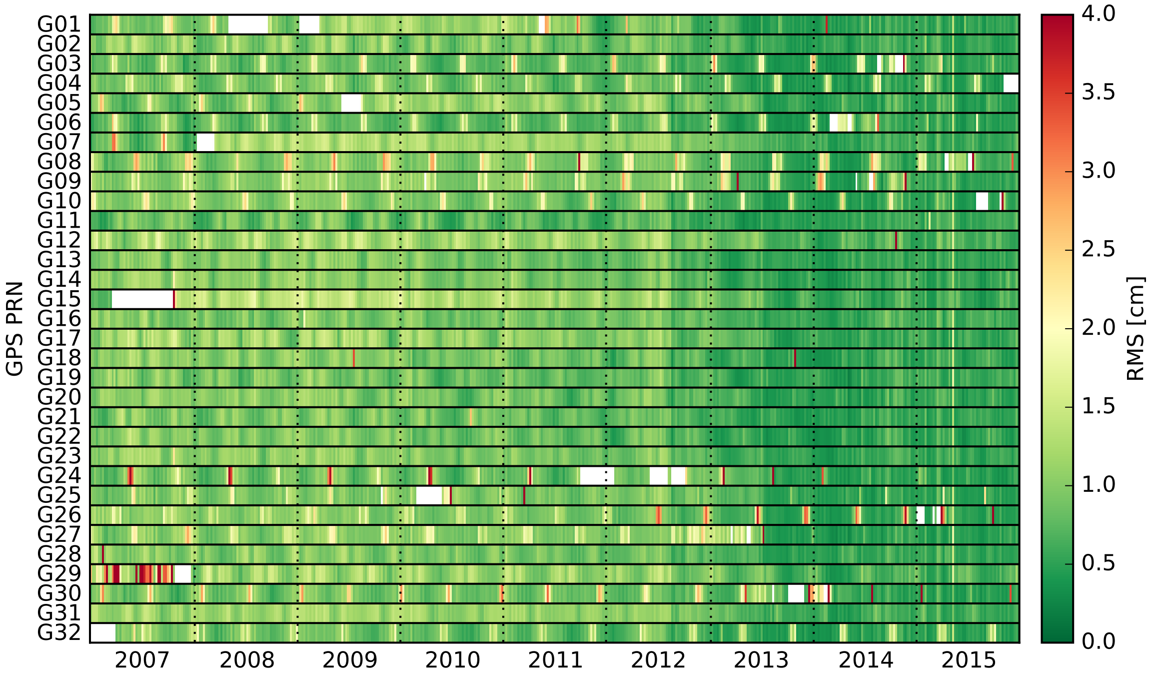

Fig. 6.3: Weekly RMS values of modeled orbits with 60 s sampling compared to IGS final orbits over the full analysis period. The pattern with increased RMS values during eclipse season disappeared for all but block IIA satellites. The issues with block IIA satellites are related to their unreliable behavior during shadow crossings. From late 2012 onwards, the fit to IGS orbits visibly improves for all satellites, which may be related to the introduction of IGb08.

is negative due to the axis definition of the ECOM, where the D-axis points from the satellite to the Sun and therefore opposite to photon flow direction. The cosine two-per-revolution and four-per-revolution terms D_{C2} and D_{C4} show a large bias-like deviation during eclipse seasons. These deviations may be related to the treatment of shadow crossings, where the corresponding entries of the solar radiation pressure parameters in the design matrix are multiplied with a factor derived from a conical shadow model. If a satellite is in full shadow, the corresponding design matrix entries are therefore set to zero. Since the parameters are estimated once per 24-hour arc, two shadow crossings with a peak length of about an hour may have a greater influence on parameters like the two-per-revolution and four-per-revolution terms that model higher frequency effects. However, further investigations into this issue are required.

Outside eclipse season there is no benefit of a 60 s sampling compared to 300 s and therefore it would potentially be possible to limit the higher sampling rate to the shadow crossings. This would result in a reduction of computation time and storage space requirements, but this reduction is arguably insignificant.

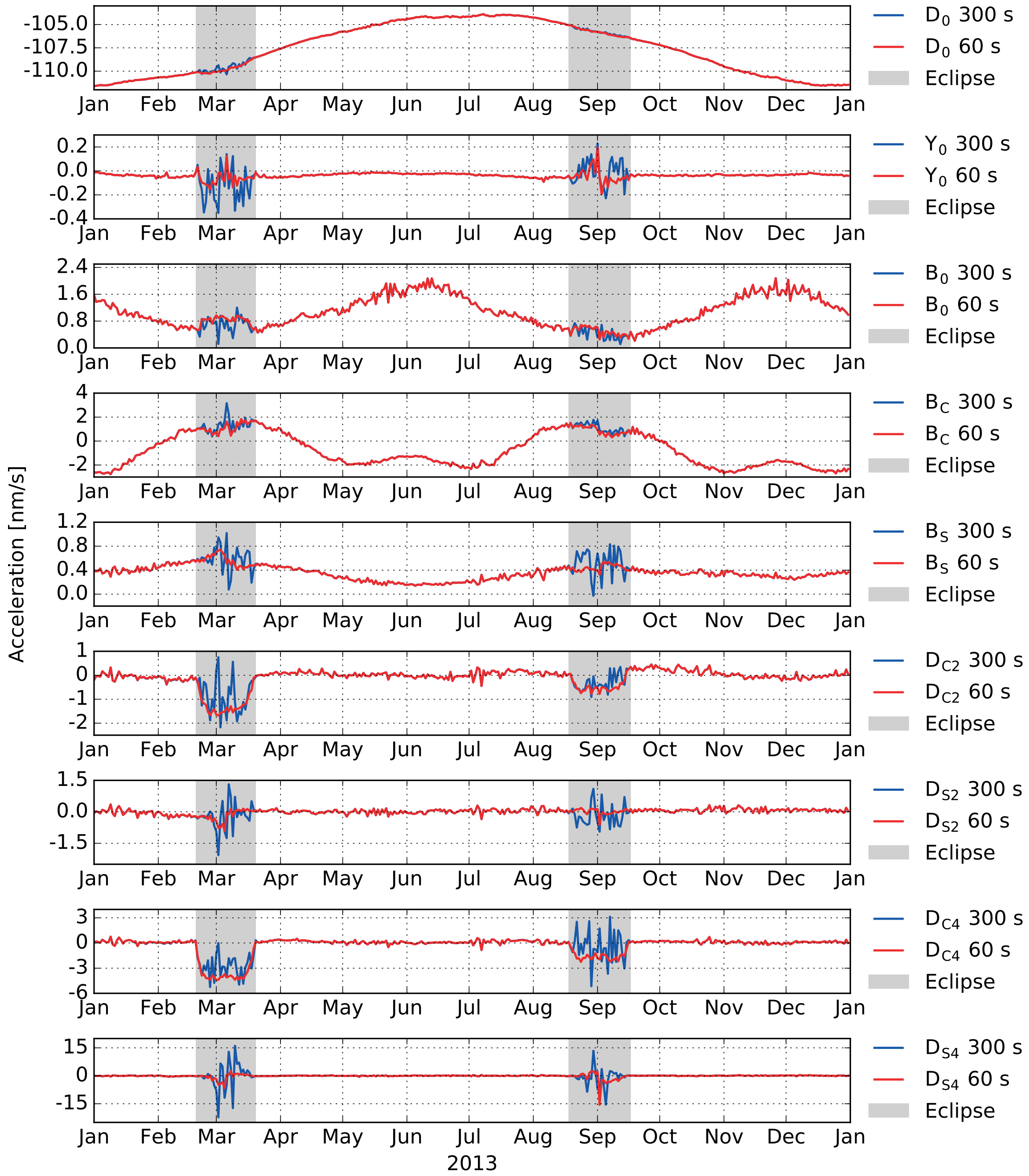

Fig. 6.4: ECOM9N solar radiation pressure parameters estimated during orbit modeling of GPS satellite G01 in 2013. During eclipse seasons (gray areas), orbit modeling with a 60 s sampling (red) results in significantly more stable estimates than with 300 s (blue). However, even with 60 s there are still deviations during eclipse seasons, which indicate further deficiencies in orbit modeling. The direct term D_0 is by far the largest term and shows correlation to the distance between the satellite/Earth and the Sun. The largest acceleration occurs at perihelion in early January and the smallest acceleration at aphelion in early July (negative due to axis definition).

6.2 Data, models, and settings

In the conducted analyses GPS observations from the global IGS permanent station network were processed to determine orbits for the full GPS constellation. The IGS station network consists of more than 400 stations with a very uneven distribution (see Figure 2.2, page 5). While the station density in Europe, North America and East Asia is very high, it is lacking on the southern hemisphere and, naturally, on the oceans. The IGb08 core network, shown in Figure 6.5, is a well-distributed subset of the full IGS network. This subset of 91 stations was chosen to reduce the number of stations to process while maintaining a globally even distribution. In general, IGb08 is an adaption of the IGS08 reference frame, which in turn is the IGS realization of the International Terrestrial Reference Frame 2008 (ITRF2008) (Rebischung et al., 2011). The adaption was necessary due to the retirement of a number of permanent stations over time, which was especially problematic for the core network.

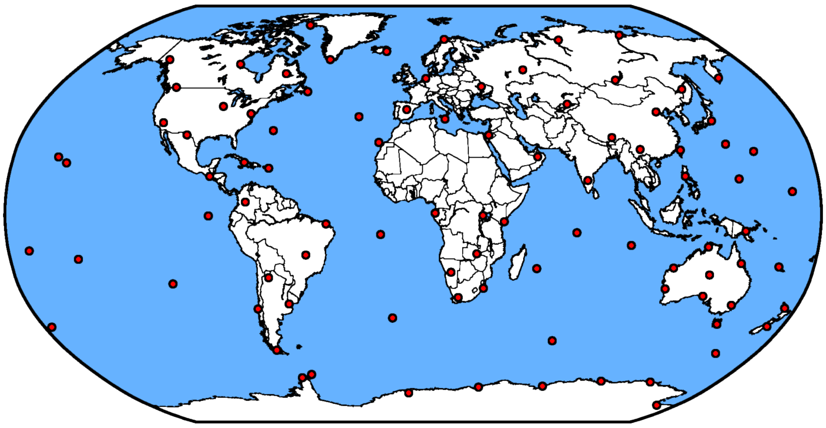

Fig. 6.5: Station distribution of the IGb08 core network

Figure 6.6 illustrates the number of stations that were actually used on each day of the analyzed 9-year period. The station count per day is lower that the total station count of the IGb08 core network due to temporary outages or permanent retirements of stations without substitutes. Stations are also excluded during processing if they exhibit a large amount of outliers or a low number of observed epochs or satellites. On average, 67 stations were processed per day to determine the orbits of 31 operational GPS satellites. The observation types utilized in

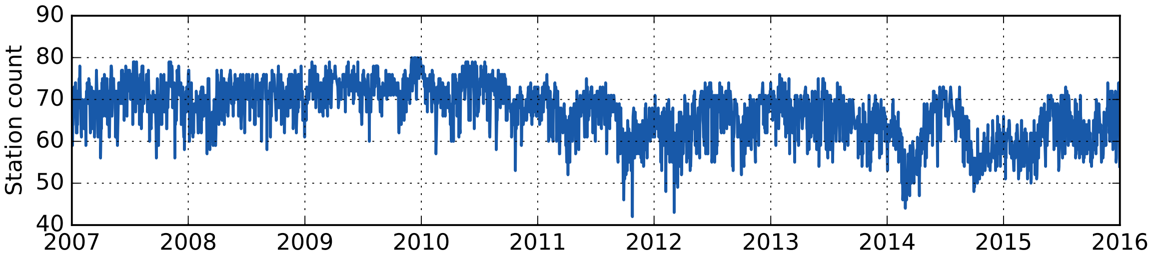

Fig. 6.6: Daily number of processed stations from the IGb08 core network. On average, observations from 67 stations were processed per day.

the analyses were limited to code and phase observations on the L1 and L2 frequency bands. Each observation type is provided with a sampling of 30 s by the station operators. With 67 stations, 31 satellites, and an elevation cutoff of 5° this leads to approximately 1.7 million observations per observation type and day, which amounts to a daily average of roughly 6.8 million observations. In total, around 22 billion observations have been processed over the analyzed period from 2007 to 2015. All orbit determination processing was performed at the observation sampling of 30 s.

On the satellite side, IGS final orbits with a sampling of 15 min have been used as reference orbits during orbit modeling. IGS final clock products with a sampling of 30 s served as approximate clock errors. Satellite information and phase center variations for both receiver and transmitter antennas were taken from the ANTEX file provided by the IGS. Code observations were corrected using differential code biases determined by the Center for Orbit Determination in Europe. A no-net-rotation constraint was applied to the satellite orbits. This was necessary to prevent a datum defect, since both satellite orbits and station positions were estimated and therefore the whole system could be freely rotated without affecting the relative observations. A stochastic pulse was also added at the center of each daily arc. This instantaneous velocity change was constrained to zero with a standard deviation of $10^{-4}\,\mathrm{m/s}$. Nominal satellite orientations were used at all times, including shadow crossings. Additions to the initial state vector and the parameters of the ECOM9N solar radiation pressure model were estimated during orbit determination to improve the fit of the modeled orbit to the observations. Satellite clock errors were estimated for each epoch as well.

On the station side, approximate coordinates, receiver information, and antenna information were taken from the station log files provided by the station operators via the IGS. A priori standard deviations for code and phase observations depend on the zenith angle z via

$$\sigma_0 = \frac{\sigma_{\text{zenith}}}{\cos z} \tag{6.1}$$

and were computed using $\sigma_{\text{zenith}} = 20\,\mathrm{cm}$ for code and $\sigma_{\text{zenith}} = 2\,\mathrm{mm}$ for phase observations. The models used to compute station displacements are listed in Table 6.1. Station positions were estimated constant per day and receiver clock errors once per epoch using the 30 s sampling. The troposphere was modeled using the Vienna Mapping Functions 1 (VMF1) (Boehm et al., 2006). Additionally, residual wet delays were estimated once per hour using a first-degree spline. Horizontal delay gradients were also estimated at the beginning and end of each day using a first-degree spline with a sampling of 24 h. Earth rotation was modeled based on the IERS 2010 conventions (Petit and Luzum, 2010) using the Earth orientation parameters from EOP 08 C04 series provided by the IERS. Float ambiguities were estimated for continuous tracks of phase observations on both frequencies, which amounts to approximately 5400 tracks or 10 800 ambiguities per day. Table 6.2 lists the average number of estimated parameters per day using 67 stations, 31 satellites, and a sampling of 30 s.

Tab. 6.1: Models used to compute station displacements

Effect	Model	Reference
Solid Earth tides	IERS 2010	Petit and Luzum (2010)
Ocean tides	EOT11a	Savcenko and Bosch (2012)
Global mass variations	AOD1B RL05	Dobslaw et al. (2013)
Pole tide	IERS 2010	Petit and Luzum (2010)
Ocean pole tide	IERS 2010	Petit and Luzum (2010)

Tab. 6.2: Daily number of estimated parameters using an average of 67 stations, 31 satellites, and 2880 epochs per day

Parameter type	Parameter count	Daily average
Satellite initial state	6 per day and satellite	186
Satellite clock error	1 per epoch and satellite	89 280
Solar radiation pressure	9 per day and satellite	279
Ambiguity	2 per track	10 800
Slant TEC	1 per observation quadruple	1 700 000
Tropospheric wet delay	25 per day and station	1625
Tropospheric gradient delay	4 per day and station	268
Station position	3 per day and station	201
Station clock error	1 per epoch and station	192 960
Average total parameter count per day		**1 995 599**

Over the analyzed period from 2007 to 2015, the daily average of 2 million parameters adds up to approximately 6.5 billion parameters. These parameters are estimated from an average of 6.8 million observations per day or around 22 billion in total over the analysis period, as mentioned above.

6.3 Results and validation

Figure 6.7 compares the overall quality of the determined orbits against the reference IGS final orbits in terms of weekly RMS values. The orbits determined by the Center for Orbit Determination in Europe (CODE), European Space Agency (ESA), and Jet Propulsion Laboratory (JPL) are also shown for reference and validation. IGS analysis centers produce GPS orbits on a daily basis in their routine processing, which are then combined to the IGS final orbits. Therefore, these orbits represent the models and methods that were deemed state-of-the-art at the time of their processing. Up to the end of 2013, reprocessed orbits are provided by the IGS analysis centers, which were computed for the second IGS reprocessing campaign using updated models and methods. Since the orbits determined within the scope of this thesis are technically reprocessed orbits as well, the reprocessed analysis center orbits were used to ensure a fair comparison. From 2014 onwards the routinely processed orbits of the analysis centers were used. This is clearly visible in Figure 6.7 by the increased amount of noise and outliers in the weekly RMS values of the analysis centers. The original IGS final orbits had to be used as reference over the complete analysis period since there is no new combination of

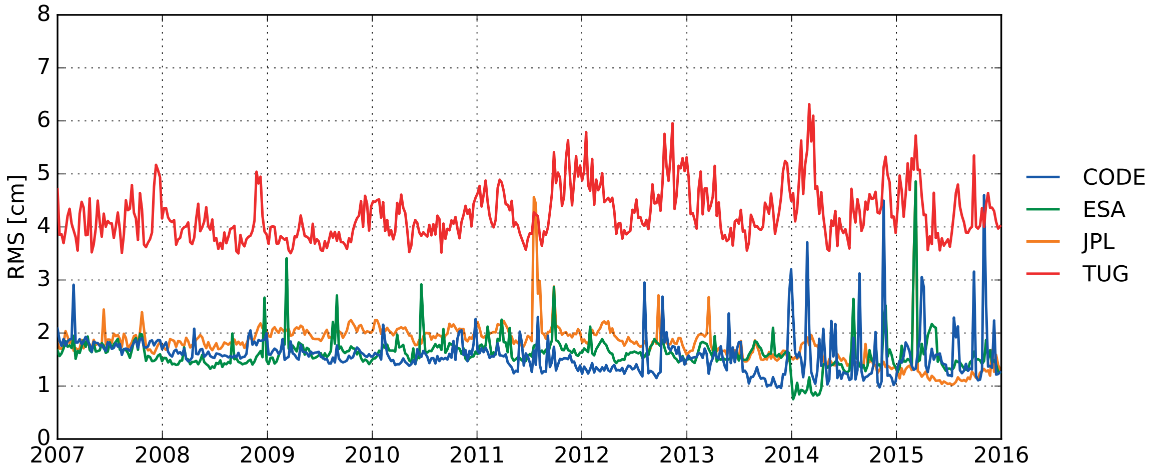

Fig. 6.7: Weekly RMS values of the determined orbits (red) and of the orbits by the IGS analysis centers CODE (blue), ESA (green), and JPL (orange) compared to the reference IGS final orbits. The analysis center orbits are reprocessed orbits up to the end of 2013 and routinely processed orbits afterwards, which is noticeable by the increased amount of noise and outliers. The overall RMS of the determined orbits is around 4 cm compared to the orbits of the analysis centers with an overall RMS of about 2 cm.

the reprocessed analysis center orbits. As Figure 6.7 shows, the overall RMS of the determined orbits is around 4 cm compared to the reference IGS final orbits. The orbits of the IGS analysis centers lead to an RMS of about 2 cm. It has to be noted though that the IGS final orbits are a combination of the analysis center orbits and therefore they will inevitably compare well to the combination. This is not directly the case for the reprocessed orbits but the respective original analysis center orbits are still part of the combination. In general, the results indicate that the raw observation approach is definitely applicable to GNSS orbit determination. However, there is still much room for further improvements to get results comparable to the currently established approaches used by the IGS analysis centers.

Investigating the results in more detail reveals that the weekly RMS values are generally around 3–4 cm for the individual satellites, as illustrated by Figure 6.8. During certain and to some extent recurring periods the RMS values significantly increase. Some of these periods correlate to those with increased RMS values in orbit modeling (see Figure 6.3, page 38), which indicates insufficiencies in orbit modeling rather than during the processing itself. Examples for these orbit modeling issues are G29 in 2007 or the solar radiation pressure modeling issues of block IIA satellites, e.g. G24 up to 2011. The issues of block IIA satellites are presumably related to modeling the satellite attitude during shadow crossings, as discussed in Section 6.1.

Other problematic periods, e.g. G01 from 2008 to 2011 and G32 in 2007, are related to changes in the GPS constellation and the status of the involved satellites. From 2008 to 2011 several different satellites were assigned to PRN code G01, and the signal was set to an unhealthy status for most of this period. The same applies to G32, which was launched in late

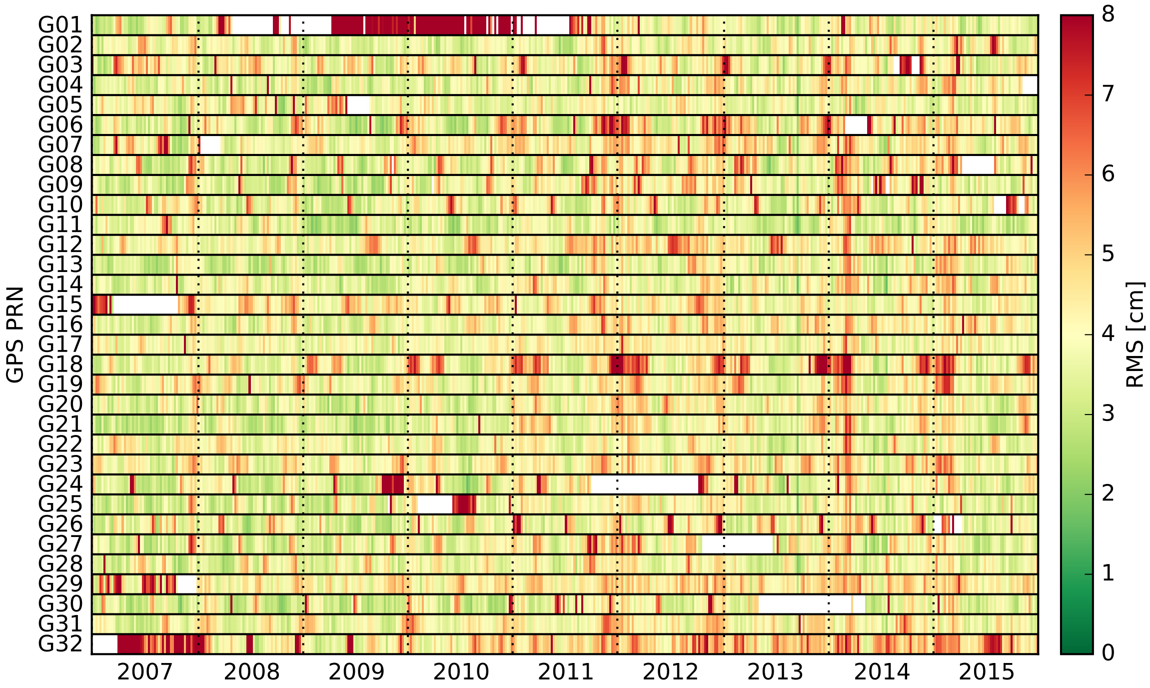

Fig. 6.8: Weekly RMS values of the determined orbits per satellite compared to the reference IGS final orbits. While the RMS values are generally around 3–4 cm, certain and to some extent recurring periods show significantly increased RMS values. Some of these periods, e.g. G29 in 2007, are related to orbit modeling deficiencies. Other problematic periods, e.g. G01 from 2008 to 2011 and G32 in 2007, originate in GPS constellation changes and satellites with unhealthy signal status.

2006 and was set to unhealthy for most of 2007. The IGS generally also processes unhealthy satellites, although not all ground stations track these satellites and the observations may be unreliable. As the results in Figure 6.8 show, processing unhealthy satellites is problematic with the current software implementation and severely degrades the determined orbits. The issues most likely originate from the rudimentary observation preprocessing that is currently implemented. Outlier and cycle slip detection and related steps like ambiguity track definition require further work and offer much room for improvement in the future.

The increased overall RMS values in Figure 6.7 that are noticeable around the turns of the years, especially from 2011 onwards, evidently stem from only a few satellites with increased RMS values at these periods, e.g. G06 and G18. Figure 6.9 shows the updated ECOM9N solar radiation pressure parameters estimated during orbit determination compared to those estimated during orbit modeling for satellite G18 in 2012. During some periods, the updated solar radiation pressure parameters deviate significantly from those estimated during orbit modeling, even outside the eclipse seasons. Especially B_C and D_{C2} show large deviations at the beginning and end of the year. However, it has yet to be determined if the issues that appear for some satellites around the turns of the years originate from solar radiation pressure modeling or if the estimated parameters just absorb the effects of unrelated issues.

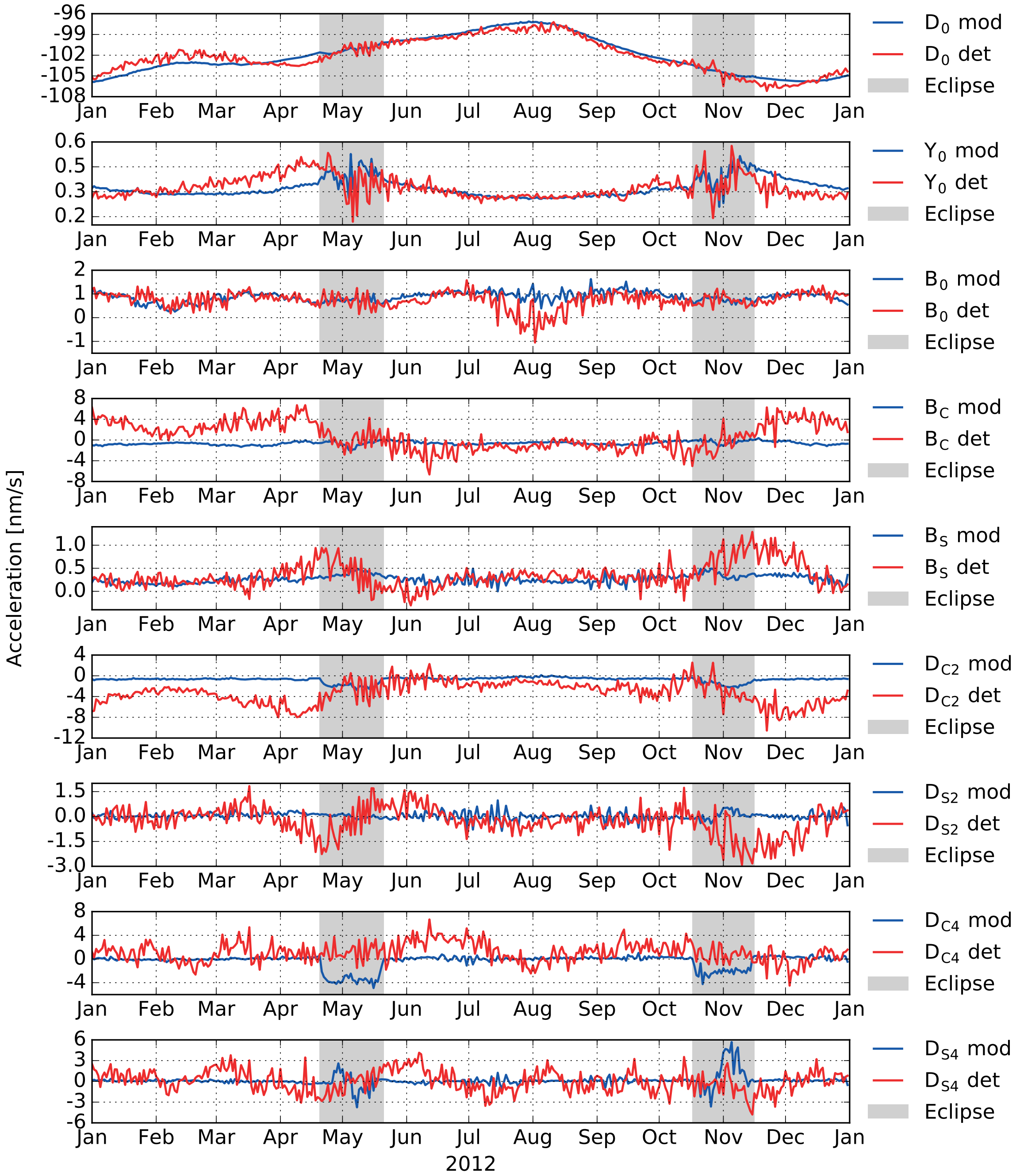

Fig. 6.9: Estimated ECOM9N solar radiation pressure parameters for GPS satellite G18 in 2012. The updated parameters from orbit determination (red) deviate significantly from the parameters estimated during orbit modeling (blue) for some periods. The parameters B_C and D_{C2} show large deviations even outside eclipse seasons (gray area) at the beginning and end of the year. It has yet to be determined if these deviations originate from solar radiation pressure modeling issues or if they are connected to unrelated issues that are simply absorbed by the estimated parameters.

Summary and outlook

7

The objective of this thesis was the adaption of the raw observation approach (Zehentner and Mayer-Gürr, 2014) to precise orbit determination of GNSS satellites. In the first part, orbit modeling and all conservative and nonconservative forces that affect GNSS satellite orbits have been described. Numerical analyses were conducted over a period from 2007 to 2015 to identify the effects these forces have on real GPS orbits. The results showed that small conservative forces like global mass variations, pole tide, and ocean pole tide are negligible. Nonconservative forces on the other hand have a significant impact on GPS orbits, especially the parametrization of solar radiation pressure. Here, the analyses confirmed the importance of modeling two-per-revolution and four-per-revolution terms when using the empirical CODE orbit model (ECOM).

The second part of this thesis focused on the raw observation approach itself and how to fit the modeled orbits to GNSS observations. The modeling and parametrization of all influences that have to be considered when using the raw observation approach have been described in detail. To test the approach, orbits of the GPS constellation have been determined over a period of nine years from 2007 to 2015 using observations from a global network of IGS permanent stations. The results demonstrated that the raw observation approach is applicable to orbit determination of GNSS satellites. However, it is not quite yet at the level of well-established approaches used by IGS analysis centers. Nonetheless, the work conducted within the scope of this thesis forms a good foundation to be built on and there is still much room for future improvements.

The analyses showed some deficiencies in orbit modeling, mostly related to solar radiation pressure modeling during eclipse seasons, that require further investigations. Processing observations from satellites with an unhealthy status appears to be problematic with the current software implementation due to unreliable observations and a reduced number of stations that track these satellites. Further work is therefore needed to improve observation preprocessing, especially outlier and cycle slip detection. For some satellites the quality of the determined orbits deteriorates during specific periods. It has yet to be determined if this is related to solar radiation pressure modeling or if it has other causes. Significant improvements to the determined orbits can be expected if the estimated float ambiguities are fixed to integer values. However, undifferenced integer ambiguity resolution is a nontrivial topic due to the presence of phase biases and therefore requires further investigations in the future.

Abbreviations

ANTEX	Antenna exchange
AOD1B	Atmosphere and Ocean De-aliasing Level 1B
AU	Astronomical unit
CDMA	Code division multiple access
CERES	Clouds and the Earth’s Radiant Energy System
CGCS2000	China Geodetic Coordinate System 2000
CHAMP	Challenging Minisatellite Payload
CODE	Center for Orbit Determination in Europe
ECOM	Empirical CODE orbit model
EGM2008	Earth Gravitational Model 2008
EGNOS	European Geostationary Navigation Overlay Service
EMR	Natural Resources Canada
EOP	Earth orientation parameter
EOT11a	Empirical Ocean Tide model 2011a
ESA	European Space Agency
ESOC	European Space Operations Centre
FDMA	Frequency division multiple access
FES2004	Finite Element Solution 2004
FOC	Full operational capability
GCRS	Geocentric Celestial Reference System
GEO	Geostationary orbit
GFZ	GeoForschungsZentrum
GLONASS	Globalnaya Navigatsionnaya Sputnikovaya Sistema
GNSS	Global navigation satellite system
GOCE	Gravity field and steady-state Ocean Circulation Explorer
GOCO05s	Gravity Observation Combination 05s
GOP	Geodetic Observatory Pecny

GPS	Global Positioning System
GRACE	Gravity Recovery And Climate Experiment
GRGS	Groupe de Recherche de Géodésie Spatiale
GST	Galileo System Time
GTRF	Galileo Terrestrial Reference Frame
IAGA	International Association of Geomagnetism and Aeronomy
ICGEM	International Centre for Global Earth Models
ICRS	International Celestial Reference System
IERS	International Earth Rotation and Reference Systems Service
IGRF	International Geomagnetic Reference Field
IGS	International GNSS Service
IGSO	Inclined geosynchronous orbit
IOV	In-orbit validation
IRNSS	Indian Regional Navigation Satellite System
ITRF2008	International Terrestrial Reference Frame 2008
ITRS	International Terrestrial Reference System
JPL	Jet Propulsion Laboratory
JPL DE	Jet Propulsion Laboratory Development Ephemeris
LEO	Low Earth orbit
LOD	Length of day
MEO	Medium Earth orbit
MGEX	Multi-GNSS Experiment
MIT	Massachusetts Institute of Technology
NASA	National Aeronautics and Space Administration
NGS	National Geodetic Survey
PE-90	Parameters of the Earth 1990
PPN	Parameterized post-Newtonian
PPP	Precise Point Positioning
PRN	Pseudo-random noise
RINEX	Receiver independent exchange
RMS	Root mean square
SBAS	Space-based augmentation system
SINEX	Solution independent exchange
SIO	Scripps Institution of Oceanography

SLR	Satellite laser ranging
STEC	Slant TEC
TEC	Total electron content
USNO	U.S. Naval Observatory
VMF1	Vienna Mapping Functions 1
WGS84	World Geodetic System 1984
WHU	Wuhan University

List of Figures

List of Tables

References

Arnold, D., M. Meindl, G. Beutler, R. Dach, S. Schaer, S. Lutz, L. Prange, K. Sośnica, L. Mervart, and A. Jäggi (2015). “CODE’s new solar radiation pressure model for GNSS orbit determination”. In: *Journal of Geodesy* 89.8, pp. 775–791. DOI: `10.1007/s00190-015-0814-4`.

Ashby, Neil and Bruno Bertotti (1986). “Relativistic effects in local inertial frames”. In: *Phys. Rev. D* 34 (8), pp. 2246–2259. DOI: `10.1103/PhysRevD.34.2246`.

Bar-Sever, Y. and D. Kuang (2004). “New Empirically Derived Solar Radiation Pressure Model for Global Positioning System Satellites”. In: *Interplanetary Network Progress Report* 42.159. URL: `http://ipnpr.jpl.nasa.gov/progress_report/42-159/159I.pdf`.

Barthelmes, F. and W. Köhler (2012). “International Centre for Global Earth Models (ICGEM)”. In: *Journal of Geodesy* 86.10. The Geodesist’s Handbook 2012, pp. 932–934. DOI: `10.1007/s00190-012-0584-1`.

Beutler, G., E. Brockmann, W. Gurtner, U. Hugentobler, L. Mervart, M. Rothacher, and A. Verdun (1994). “Extended orbit modeling techniques at the CODE processing center of the International GPS Service for Geodynamics (IGS)”. In: *Manuscripta Geodaetica* 19.6, pp. 367–386.

Beutler, Gerhard (2005). *Methods of Celestial Mechanics: Volume I: Physical, Mathematical, and Numerical Principles*. Springer-Verlag Berlin Heidelberg. DOI: `10.1007/b138225`.

Beutler, Gerhard, Jan Kouba, and Tim Springer (1995). “Combining the orbits of the IGS Analysis Centers”. In: *Bulletin géodésique* 69.4, pp. 200–222. DOI: `10.1007/BF00806733`.

Boehm, Johannes, Birgit Werl, and Harald Schuh (2006). “Troposphere mapping functions for GPS and very long baseline interferometry from European Centre for Medium-Range Weather Forecasts operational analysis data”. In: *Journal of Geophysical Research: Solid Earth* 111.B2. B02406. DOI: `10.1029/2005JB003629`.

China Satellite Navigation Office (2013). *BeiDou Navigation Satellite System Signal In Space Interface Control Document: Open Service Signal (Version 2.0)*. URL: `http://www.beidou.gov.cn/attach/2013/12/26/20131226b8a6182fa73a4ab3a5f107f762283712.pdf`.

Dach, Rolf, Urs Hugentobler, Pierre Fridez, and Michael Meindl (2007). *User manual of the Bernese GPS Software Version 5.0*. Astronomical Institute, University of Bern. URL: `http://www.bernese.unibe.ch/docs50/DOCU50.pdf`.

Dach, Rolf and Yoomin Jean, eds. (2013). *International GNSS Service Technical Report 2012*. Astronomical Institute, University of Bern. URL: `http://kb.igs.org/hc/en-us/article_attachments/200653858/2012_techreport-2.pdf`.

Desai, Shailen D. (2002). “Observing the pole tide with satellite altimetry”. In: *Journal of Geophysical Research: Oceans* 107.C11, pp. 7-1–7-13. DOI: `10.1029/2001JC001224`.

Dobslaw, H., F. Flechtner, I. Bergmann-Wolf, C. Dahle, R. Dill, S. Esselborn, I. Sasgen, and M. Thomas (2013). “Simulating high-frequency atmosphere-ocean mass variability for dealiasing of satellite gravity observations: AOD1B RL05”. In: *Journal of Geophysical Research: Oceans* 118.7, pp. 3704–3711. DOI: `10.1002/jgrc.20271`.

Dow, John M., R. E. Neilan, and C. Rizos (2009). “The International GNSS Service in a changing landscape of Global Navigation Satellite Systems”. In: *Journal of Geodesy* 83.3-4, pp. 191–198. DOI: `10.1007/s00190-008-0300-3`.

European Union (2010). *Galileo Open Service Signal In Space Interface Control Document (Issue 1.1)*. URL: `http://ec.europa.eu/DocsRoom/documents/11870/attachments/1/translations/en/renditions/native`.

Fliegel, H. F. and T. E. Gallini (1996). “Solar force modeling of block IIR Global Positioning System satellites”. In: *Journal of Spacecraft and Rockets* 33.6, pp. 863–866. DOI: `10.2514/3.26851`.

Fliegel, H. F., T. E. Gallini, and E. R. Swift (1992). “Global Positioning System Radiation Force Model for geodetic applications”. In: *Journal of Geophysical Research: Solid Earth* 97.B1, pp. 559–568. DOI: `10.1029/91JB02564`.

Folkner, W. M., J. G. Williams, and D. H. Boggs (2009). “The Planetary and Lunar Ephemeris DE 421”. In: *The Interplanetary Network Progress Report* 42.178, pp. 1–34. URL: `http://ipnpr.jpl.nasa.gov/progress_report/42-178/178C.pdf`.

Fritsche, M., R. Dietrich, C. Knöfel, A. Rülke, S. Vey, M. Rothacher, and P. Steigenberger (2005). “Impact of higher-order ionospheric terms on GPS estimates”. In: *Geophysical Research Letters* 32.23. L23311. DOI: `10.1029/2005GL024342`.

Ge, M., G. Gendt, M. Rothacher, C. Shi, and J. Liu (2008). “Resolution of GPS carrier-phase ambiguities in Precise Point Positioning (PPP) with daily observations”. In: *Journal of Geodesy* 82.7, pp. 389–399. DOI: `10.1007/s00190-007-0187-4`.

Geng, Jianghui, Xiaolin Meng, Alan H. Dodson, and Felix N. Teferle (2010). “Integer ambiguity resolution in precise point positioning: method comparison”. In: *Journal of Geodesy* 84.9, pp. 569–581. DOI: `10.1007/s00190-010-0399-x`.

Global Positioning Systems Directorate (2013). *GPS Interface Specification IS-GPS-200H*. URL: `http://www.gps.gov/technical/icwg/IS-GPS-200H.pdf`.

Griffiths, J. (2013). *Status of IGS Core Products*. 2013 AGU Fall Meeting. 9 December 2013, San Francisco, CA. URL: `https://www.researchgate.net/publication/264005004_Status_of_IGS_core_products`.

Hofmann-Wellenhof, Bernhard, Herbert Lichtenegger, and Elmar Wasle (2008). *GNSS – Global Navigation Satellite Systems: GPS, GLONASS, Galileo, and more*. Springer-Verlag Vienna. DOI: `10.1007/978-3-211-73017-1`.

Hofmann-Wellenhof, Bernhard and Helmut Moritz (2006). *Physical Geodesy*. 2nd ed. Springer-Verlag Wien. DOI: `10.1007/978-3-211-33545-1`.

Hoque, M. M. and N. Jakowski (2008). “Estimate of higher order ionospheric errors in GNSS positioning”. In: *Radio Science* 43.5. RS5008. DOI: `10.1029/2007RS003817`.

International GNSS Service (2015). *RINEX: The Receiver Independent Exchange Format Version 3.03*. RINEX Working Group and Radio Technical Commission for Maritime Services Special Committee 104 (RTCM-SC104). URL: `ftp://igs.org/pub/data/format/rinex303.pdf`.

International GNSS Service (2016a). *Antenna thrust values*. URL: `http://acc.igs.org/orbits/thrust-power.txt` (visited on Apr. 14, 2016).

International GNSS Service (2016b). *IGS Analysis Centers*. URL: `http://igs.org/about/analysis-centers` (visited on Apr. 14, 2016).

International GNSS Service (2016c). *IGS Products*. URL: `https://igscb.jpl.nasa.gov/components/prods.html` (visited on Apr. 14, 2016).

Jäggi, Adrian (2007). "Pseudo-stochastic orbit modeling of low Earth satellites using the Global Positioning System". In: *Geodätisch-geophysikalische Arbeiten in der Schweiz* 73. Schweizerische Geodätische Kommission. URL: `http://www.sgc.ethz.ch/sgc-volumes/sgk-73.pdf`.

Koch, K.-R. and J. Kusche (2002). "Regularization of geopotential determination from satellite data by variance components". In: *Journal of Geodesy* 76.5, pp. 259–268. DOI: `10.1007/s00190-002-0245-x`.

Kouba, J. (2009). *A Guide to Using International GNSS Service (IGS) Products*. URL: `http://igscb.jpl.nasa.gov/igscb/resource/pubs/UsingIGSProductsVer21.pdf`.

Loyer, Sylvain, Félix Perosanz, Flavien Mercier, Hugues Capdeville, and Jean-Charles Marty (2012). "Zero-difference GPS ambiguity resolution at CNES–CLS IGS Analysis Center". In: *Journal of Geodesy* 86.11, pp. 991–1003. DOI: `10.1007/s00190-012-0559-2`.

Lyard, Florent, Fabien Lefevre, Thierry Letellier, and Olivier Francis (2006). "Modelling the global ocean tides: modern insights from FES2004". In: *Ocean Dynamics* 56.5-6, pp. 394–415. DOI: `10.1007/s10236-006-0086-x`.

Maier, Andrea (2015). "Orbit determination and gravity field recovery from tracking data to geodetic satellites and the Lunar Reconnaissance Orbiter". Dissertation. Graz University of Technology.

Mayer-Gürr, T., R. Pail, T. Gruber, T. Fecher, M. Rexer, W.-D. Schuh, J. Kusche, J.-M. Brockmann, D. Rieser, N. Zehentner, A. Kvas, B. Klinger, O. Baur, E. Höck, S. Krauss, and A. Jäggi (2015). *The combined satellite gravity field model GOCO05s*. Presentation at EGU 2015, Vienna, April 2015. URL: `https://www.researchgate.net/publication/277325861_The_new_combined_satellite_only_model_GOCO05s`.

Montenbruck, O. and E. Gill (2000). *Satellite Orbits: Models, Methods and Applications*. Springer-Verlag Berlin Heidelberg. DOI: `10.1007/978-3-642-58351-3`.

Montenbruck, O., R. Schmid, F. Mercier, P. Steigenberger, C. Noll, R. Fatkulin, S. Kogure, and A.S. Ganeshan (2015). "GNSS satellite geometry and attitude models". In: *Advances in Space Research* 56.6, pp. 1015–1029. DOI: `10.1016/j.asr.2015.06.019`.

Montenbruck, O., P. Steigenberger, R. Khachikyan, G. Weber, R.B. Langley, L. Mervart, and U. Hugentobler (2014). "IGS-MGEX: Preparing the Ground for Multi-Constellation GNSS Science". In: *Inside-GNSS* 9.1, pp. 42–49. URL: `http://www.insidegnss.com/auto/janfeb14-MONTENBRUCK.pdf`.

Oleynik, Ekaterina (2012). *GLONASS Status and Modernization*. United Nations/Latvia Workshop on the Applications of Global Navigation Satellite Systems, 14–18 May 2012, Riga, Latvia. URL: `http://www.unoosa.org/pdf/sap/2012/un-latvia/ppt/1-2.pdf`.

Pavlis, Nikolaos K., Simon A. Holmes, Steve C. Kenyon, and John K. Factor (2012). "The development and evaluation of the Earth Gravitational Model 2008 (EGM2008)". In: *Journal of Geophysical Research: Solid Earth* 117.B4. B04406. DOI: `10.1029/2011JB008916`.

Petit, Gérard and Brian Luzum, eds. (2010). *IERS Conventions (2010)*. IERS Technical Note 36. Verlag des Bundesamts für Kartographie und Geodäsie, Frankfurt am Main. URL: `http://www.iers.org/IERS/EN/Publications/TechnicalNotes/tn36.html`.

Rebischung, P., J. Griffiths, J. Ray, R. Schmid, X. Collilieux, and B. Garayt (2011). "IGS08: the IGS realization of ITRF2008". In: *GPS Solutions* 16.4, pp. 483–494. DOI: `10.1007/s10291-011-0248-2`.

Rodríguez Solano, C. J. (2009). "Impact of albedo modelling on GPS orbits". Master's thesis. Technische Universität München. URL: `http://www.iapg.bgu.tum.de/mediadb/350470/350471/Thesis_CJ_Rodriguez_Solano.pdf`.

Rodríguez Solano, C. J. (2014). "Impact of non-conservative force modeling on GNSS satellite orbits and global solutions". Dissertation. Technische Universität München. URL: `http://nbn-resolving.de/urn/resolver.pl?urn:nbn:de:bvb:91-diss-20140822-1188612-0-8`.

Rodríguez Solano, C. J., U. Hugentobler, P. Steigenberger, and G. Allende-Alba (2013). "Improving the orbits of GPS block IIA satellites during eclipse seasons". In: *Advances in Space Research* 52.8, pp. 1511–1529. DOI: `10.1016/j.asr.2013.07.013`.

Russian Institute of Space Device Engineering (2008). *GLONASS Interface Control Document (Version 5.1)*. URL: `http://www.spacecorp.ru/upload/iblock/1c4/cgs-aaixymyt%205.1%20ENG%20v%202014.02.18w.pdf`.

Savcenko, R. and W. Bosch (2012). *EOT11a - Empirical Ocean Tide Model From Multi-Mission Satellite Altimetry*. DGFI Report No. 89, Deutsches Geodätisches Forschungsinstitut, Munich. URL: `http://www.dgfi.tum.de/media/docs/dgfi_reports/DGFI_Report_89.pdf`.

Shi, Junbo (2012). "Precise Point Positioning Integer Ambiguity Resolution with Decoupled Clocks". PhD thesis. University of Calgary. URL: `http://www.ucalgary.ca/engo_webdocs/YG/12.20367_JunboShi.pdf`.

Shi, Junbo and Yang Gao (2014). "A comparison of three PPP integer ambiguity resolution methods". In: *GPS Solutions* 18.4, pp. 519–528. DOI: `10.1007/s10291-013-0348-2`.

Springer, T.A., G. Beutler, and M. Rothacher (1999). "A New Solar Radiation Pressure Model for GPS Satellites". In: *GPS Solutions* 2.3, pp. 50–62. DOI: `10.1007/PL00012757`.

Springer, T.A., J.F. Zumberge, and J. Kouba (1998). "The IGS Analysis Products and the Consistency of the Combined Solutions". In: *1998 Analysis Center Workshop Proceedings*. IGS Analysis Center Workshop, Darmstadt, February 9–11, 1998, pp. 37–54. URL: `https://igscb.jpl.nasa.gov/igscb/resource/pubs/wksp.pdf`.

Švehla, D. and M. Rothacher (2005). "Kinematic Precise Orbit Determination for Gravity Field Determination". In: *A Window on the Future of Geodesy*. Ed. by Fernando Sansò. Vol. 128. International Association of Geodesy Symposia. Springer Berlin Heidelberg, pp. 181–188. DOI: `10.1007/3-540-27432-4_32`.

Swatschina, Paul (2012). "Dynamic and Reduced-Dynamic Precise Orbit Determination of Satellites in Low Earth Orbits". In: *Geowissenschaftliche Mitteilungen* 89. Department für Geodäsie und Geoinformation, Vienna. URL: `http://publik.tuwien.ac.at/files/PubDat_219297.pdf`.

Tapley, Byron D., Bob E. Schutz, and George H. Born (2004). *Statistical Orbit Determination*. Elsevier. ISBN: 978-0-12-683630-1.

Thebault, Erwan, Christopher Finlay, Ciaran Beggan, Patrick Alken, Julien Aubert, Olivier Barrois, Francois Bertrand, Tatiana Bondar, Axel Boness, Laura Brocco, Elisabeth Canet, Aude Chambodut, Arnaud Chulliat, Pierdavide Coisson, Francois Civet, Aimin Du, Alexandre Fournier, Isabelle Fratter, Nicolas Gillet, Brian Hamilton, Mohamed Hamoudi, Gauthier Hulot, Thomas Jager, Monika Korte, Weijia Kuang, Xavier Lalanne, Benoit Langlais, Jean-Michel Leger, Vincent Lesur, and Frank Lowes (2015). "International Geomagnetic Reference Field: the 12th generation". In: *Earth, Planets and Space* 67.1, p. 79. DOI: `10.1186/s40623-015-0228-9`.

Wang, K. and M. Rothacher (2013). "Ambiguity resolution for triple-frequency geometry-free and ionosphere-free combination tested with real data". In: *Journal of Geodesy* 87.6, pp. 539–553. DOI: `10.1007/s00190-013-0630-7`.

Wielicki, Bruce A., Bruce R. Barkstrom, Edwin F. Harrison, Robert B. Lee III, G. Louis Smith, and John E. Cooper (1996). "Clouds and the Earth's Radiant Energy System (CERES): An Earth Observing System Experiment". In: *Bulletin of the American Meteorological Society* 77, pp. 853–868. DOI: `10.1175/1520-0477(1996)077<0853:CATERE>2.0.CO;2`.

Zehentner, N. and T. Mayer-Gürr (2014). "New Approach to Estimate Time Variable Gravity Fields from High-Low Satellite Tracking Data". In: *Gravity, Geoid and Height Systems*. Ed. by Urs Marti. Vol. 141. International Association of Geodesy Symposia. Springer International Publishing, pp. 111–116. DOI: `10.1007/978-3-319-10837-7_14`.

Zehentner, N. and T. Mayer-Gürr (2015). "Precise orbit determination based on raw GPS measurements". In: *Journal of Geodesy*, pp. 1–12. DOI: `10.1007/s00190-015-0872-7`.

Zhao, Qile, Binzi Sun, Zhiqiang Dai, Zhigang Hu, Chuang Shi, and Jingnan Liu (2015). "Real-time detection and repair of cycle slips in triple-frequency GNSS measurements". In: *GPS Solutions* 19.3, pp. 381–391. DOI: `10.1007/s10291-014-0396-2`.